

Fredrik Gran-Jansen

# Hyperspectral data analysis for chlorophyll estimation and operation of HYPSON-1 satellite

Master's thesis in Cybernetics and Robotics

Supervisor: Tor Arne Johansen

Co-supervisor: Joseph L. Garrett

July 2022



Fredrik Gran-Jansen

# **Hyperspectral data analysis for chlorophyll estimation and operation of HYPSON-1 satellite**



Master's thesis in Cybernetics and Robotics  
Supervisor: Tor Arne Johansen  
Co-supervisor: Joseph L. Garrett  
July 2022

Norwegian University of Science and Technology  
Faculty of Information Technology and Electrical Engineering  
Department of Engineering Cybernetics



Norwegian University of  
Science and Technology



---

## Abstract

HYPer-spectral Smallsat for ocean Observation (HYPSO) launched the satellite HYPSO-1 into orbit on the 13th of January, 2022. The satellite captures ocean color with hyperspectral remote sensing by separating light in the visible to near-infrared spectrum into many separate spectral bands. Thus, increasing the information we receive from an image. This thesis presents and conducts methods of operation on the HYPSO-1 satellite, such as mission planning, communication, and system observations. Operations proved to meet most of the requirements studied in this thesis. However, mission planning for several days in advance resulted in inaccurate timestamps and attitudes as HYPSO-1's orbital elements must be updated regularly. Thus, automated mission planning with e.g., Satellite Operations User Interface Enhancement Suite (SOUIES), is necessary to reduce manual labor and errors. With high bit-rate down-linking of housekeeping telemetry and logs, the operators could regularly observe the satellite's health and troubleshoot any problems. By observing the system's battery voltage, it is estimated that the satellite meets its life expectancy.

The next part presents data processing techniques such as calibration, radiance to reflectance conversion, dimensionality reduction, and unsupervised classification with k-means. These techniques are applied to hyperspectral data acquired over Frohavet in Norway to estimate algae concentrations. Radiometric and spectral calibration were conducted, however, corrections for atmospheric effects and Smile and Keystone were not available. Principal component analysis and classification did not detect algae as they suffered from limitations due to the brief period the satellite had been in orbit. However, dimensionality reduction with principal component analysis and clustering with classification proved to be successful. Acquisition of correct georeferencing, solar zenith angle per pixel, solar spectral irradiance per wavelength, atmospheric corrections, and removal of camera defects were not available at the time of writing. Methods to work around these limitations are presented to achieve adequate results that can be analyzed, and suggested future work is presented in the conclusion section.

After acquiring and analyzing a vast amount of captures, we chose one hyperspectral image over Frohavet to be presented and analyzed in this thesis. With this capture we will attempt to answer how well HYPSO meets the satellite operation needs from an end-to-end perspective and if the acquired data are successfully calibrated and usable for end-users. It is necessary to investigate where HYPSO needs to put resources to satisfy specific requirements and whether these requirements should be updated for the HYPSO-2 satellite or not.

---

## Sammendrag

HYPISO skjøt opp satellitten HYPISO-1 i bane 13. Januar 2022. Satellitten fanger havfarger med hyperspektral fjernmåling ved å separere lys i det synlige til nær-infrarøde spekteret i mange separate spektralbånd. Dermed øker informasjonen vi mottar fra et bilde. Denne masteroppgaven presenterer og gjennomfører operasjonsmetoder på HYPISO-1 satellitten, som f.eks oppdragsplanlegging, kommunikasjon og systemobservasjoner. Satellittoperasjonene viste seg å møte de fleste av kravene som er studert i denne oppgaven, men oppdragsplanlegging for flere dager i forveien resulterte i unøyaktig tidsstempler og retningskontroll siden HYPISO-1 sine orbitale elementer må oppdateres regelmessig. Dermed er automatisert oppdragsplanlegging med for eksempel SOUIES nødvendig for å redusere manuelt arbeid og feil i dataen. Med høy nedkoblings bithastighet av telemetri og logger kunne operatører regelmessig observere satellittens helse og feilsøke eventuelle problemer. Ved å observere systemets batterispenning, anslås det at satellitten når sin forventede levetid.

Den neste delen presenterer databehandlingsteknikker som kalibrering, utstråling til reflektans konvertering, dimensjonalitetsreduksjon og uovervåket klassifisering med «k-means» algoritmen. Disse teknikkene brukes på hyperspektral data innhentet over Frohavet i Norge for å estimere algekonsentrasjoner. Radiometrisk og spektral kalibrering ble utført, mens korreksjoner for atmosfæriske effekter og "Smile" og "Keystone" var ikke tilgjengelige. Hovedkomponentanalyse og klassifisering oppdaget ikke alger da de led av begrensninger på grunn av den korte perioden satellitten hadde vært i bane. Derimot viste dimensjonalitetsreduksjon med hovedkomponentanalyse og klynging ved klassifisering seg å være vellykket. Innhenting av korrekt georeferering, solens senitvinkel per piksel, solens spektrale irradians per bølgelengde, atmosfæriske korreksjoner og fjerning av kameradefekter var ikke tilgjengelig i skrivende stund. Metoder for å omgå disse begrensningene presenteres for å oppnå tilstrekkelige resultater som kan analyseres, og foreslått fremtidig arbeid presenteres i konklusjonsdelen.

Etter å ha anskaffet og analysert en stor mengde hyperspektrale bilder, valgte vi ett hyperspektralt bilde over Frohavet som presenteres og analyseres i denne oppgaven. Med dette bildet vil vi forsøke å svare på hvor godt HYPISO dekker satellittoperasjonsbehovet fra et ende-til-ende-perspektiv og om de innhentede dataene er vellykket kalibrert og brukbare for sluttbrukere. Det er nødvendig å undersøke hvor HYPISO trenger å sette inn ressurser for å tilfredsstille spesifikke krav, og om disse kravene bør oppdateres for HYPISO-2-satellitten eller ikke.

---

## Preface

In the summer of 2021, I applied as a research assistant for HYPSON as a Cybernetics and Robotics Master's student at the Norwegian University of Science and Technology (NTNU). The opportunity to work on a satellite as a 24-year-old was a lifelong dream and I quickly signed up to write my Project thesis about HYPSON's hyperspectral imager (HSI). I was later allowed to write my Master's thesis for HYPSON about the same topic, only this time, the HSI was attached to the HYPSON-1 satellite and launched into orbit.

I was integrated into satellite operations to be the first person to go through planning, acquiring, and analyzing a capture. Thus, I was able to investigate where HYPSON needed to put more resources and whether the research requirements were fulfilled or not. As the HYPSON team had been working on the satellite since 2018, I had to acquire knowledge about satellite operations through scripts already made for mission planning and communication with the satellite through command-line interfaces (CLI). I could observe the satellite's housekeeping telemetry through Grafana and plan missions with the software Systems Tool Kit (STK). I also acquired georeferenced data from Dennis D. Langer and calibration scripts from Marie Henriksen that were applied to the raw hyperspectral data. These efforts form the basis of the thesis.

The hyperspectral data was analyzed with SNAP and Excel, as they function as great tools for analyzing, processing, and visualizing hyperspectral data. Through research and input from my co-supervisor, Joseph Garret, I learned about these data processing techniques, which expanded my knowledge about hyperspectral data.

As I started my Master's thesis shortly after launch, certain limitations made the work more challenging. Several measurements were unavailable from HYPSON at the time, thus increasing the need to understand alternative methods. For instance, radiance to reflectance conversion was especially challenging as the variables had to be estimated from other sources.

The point of the thesis was to tie everything together, end-to-end, and learn the process of planning a capture to analyze it. I have been a part of the satellite operation team for several months, acquiring and analyzing a vast amount of data for HYPSON. Weekly troubleshooting of operational errors and discussions about alternative measurements with several researchers and students created a fantastic arena for obtaining knowledge and connecting with people. It has been a valuable experience for me and the HYPSON team.

Thank you.

Trondheim, July 11, 2022

*Fredrik Gran-Jansen*

Fredrik Gran-Jansen

---

## Acknowledgement

This master's thesis was written in cooperation with the NTNU HYPSON team. Special thanks to my co-supervisor, Joseph Garret, for proofreading and taking your time each week to meet up and discuss my thesis and progress. I want to thank Tor Arne Johansen for allowing me to write my master's thesis for such an inspiring team and project. Additional thanks to Dennis D. Langer, Sivert Bakken, Marie Henriksen, Elizabeth F. Prentice, and Bjørn A. Kristiansen, who shared opinions, documents, and measurements relevant to my thesis. Thank you, Simen Berg and Roger Birkeland, for your commitment to sharing your knowledge about satellite operations and always being available for support. I also want to thank Roger and Evelyn Honoré-Livermore for including me in weekly operation meetings and integrating me into the HYPSON team. I must thank Esmée Oudijk, who accompanied me through satellite operations training, and for always being in such a great mood. Lastly, I want to thank my family, friends, and partner for supporting me through my years at NTNU.

F.G.J

### Remark:

Thanks to Emeritus Marvin Rausand for creating the  $\text{\LaTeX}$  template used in this thesis.



---

# Acronyms

<b>ADCS</b>	Attitude determination and control system
<b>AER</b>	Azimuth, elevation, and range
<b>AOS</b>	Acquisition of Signal
<b>ASV</b>	Autonomous Surface Vehicles
<b>AUV</b>	Autonomous Underwater Vehicles
<b>CAN</b>	Controller Area Network
<b>CDOM</b>	Colored dissolved organic matter
<b>CLI</b>	Command-line interfaces
<b>CMOS</b>	Complementary Metal-Oxide-Semiconductor
<b>CONOPS</b>	Concepts of operation
<b>CSP</b>	CubeSat Space Protocol
<b>CSV</b>	Comma-separated values files
<b>EPS</b>	Electrical Power System
<b>FC</b>	Flight Computer
<b>FOV</b>	Field Of View
<b>HSI</b>	Hyperspectral Imager
<b>HYPSO</b>	HYPer-spectral Smallsat for ocean Observation
<b>HYPSO-1</b>	The first HYPSO SmallSat
<b>HYPSO-2</b>	The second HYPSO SmallSat
<b>IMU</b>	Inertial Measurement Unit
<b>L1A</b>	Level 1A
<b>LOS</b>	Loss of Signal
<b>LV LH</b>	Local-Vertical-Local-Horizontal
<b>MSE</b>	Mean-squared error
<b>NTNU</b>	Norwegian university of science and technology
<b>OCR</b>	Ocean Color Radiance
<b>OPU</b>	Onboard Processing Unit
<b>PC</b>	Payload Controller
<b>PCA</b>	Principal Component Analysis
<b>RGB</b>	Red, Blue and Green

---

**ROI** Region of interest

**SNAP** Sentinels Application Platform

**SOUIES** Satellite Operations User Interface Enhancement Suite

**STK** Systems Tool Kit

**TLE** Two Line Element

**ToA** Top of Atmosphere

**UAV** Unmanned Aerial Vehicles

**UHF** Ultra-High-Frequency

**VIS-NIR** Visible–Near–Infrared

---

# Contents

<b>Abstract</b>	<b>i</b>
<b>Sammendrag</b>	<b>ii</b>
<b>Preface</b>	<b>iii</b>
<b>Acknowledgement</b>	<b>iv</b>
<b>Acronyms</b>	<b>v</b>
<b>1 Introduction</b>	<b>1</b>
1.1 Motivation . . . . .	1
1.2 Previous work . . . . .	1
1.3 Thesis Objectives and Contributions . . . . .	2
1.3.1 Thesis Objectives . . . . .	2
1.3.2 Thesis Contributions . . . . .	4
1.4 Thesis Outline . . . . .	4
<b>2 Theory of hyperspectral remote sensing</b>	<b>5</b>
2.1 Overview of remote sensing . . . . .	5
2.2 Hyperspectral imaging . . . . .	5
2.3 Camera . . . . .	5
2.3.1 Design of the HSI . . . . .	5
2.3.2 Pushbroom scanning . . . . .	6
2.4 Ocean color . . . . .	7
2.4.1 Why do we look for phytoplankton? . . . . .	8
2.4.2 Chlorophyll-a . . . . .	8
2.5 Spectral calibration . . . . .	9
2.5.1 Stray light . . . . .	9
2.5.2 Smile and keystone correction . . . . .	9
2.5.3 Atmospheric correction . . . . .	10
2.5.4 Calibrating a real camera . . . . .	10
2.6 Classification of hyperspectral images . . . . .	12

---

2.6.1	K-means algorithm . . . . .	12
2.7	PCA . . . . .	13
2.8	Radiance to reflectance . . . . .	15
2.8.1	Solar zenith angle . . . . .	16
<b>3</b>	<b>Theory of operations</b>	<b>17</b>
3.1	CONOPS . . . . .	17
3.2	HYPSONO-1 system . . . . .	18
3.2.1	Satellite Bus . . . . .	18
3.2.2	Attitude Determination and Control System . . . . .	19
3.2.3	EPS . . . . .	20
3.2.4	Payload Controller (PC) and Flight Computer (FC) . . . . .	21
3.3	Communication . . . . .	21
3.3.1	NanoMCS and hypso-cli . . . . .	21
3.3.2	Generating PC and FC scripts . . . . .	21
3.3.3	Up-link and down-link through the S-band . . . . .	21
3.4	Mission planning . . . . .	22
3.4.1	Timing - PC/FC scripting . . . . .	22
3.4.2	Quaternions . . . . .	22
<b>4</b>	<b>Experimental setup</b>	<b>24</b>
4.1	Order of operations . . . . .	24
4.1.1	Preparations for observing a scene . . . . .	24
4.1.2	Target capture planning with STK . . . . .	24
4.1.3	Quaternions . . . . .	27
4.1.4	Generating PC and FC scripts . . . . .	27
4.1.5	Scheduling and upload . . . . .	27
4.1.6	Grafana - before and after a pass . . . . .	28
4.1.7	During a pass . . . . .	31
4.1.8	Pull from nanoMCS . . . . .	33
4.1.9	Delete safe copies and download logs . . . . .	33
4.1.10	Georeferencing . . . . .	34

---

---

4.2	Analysis . . . . .	36
4.2.1	Startup . . . . .	36
4.2.2	Masking . . . . .	37
4.2.3	Unsupervised classification and PCA . . . . .	38
4.2.4	Radiance to reflectance . . . . .	39
<b>5</b>	<b>Results</b>	<b>40</b>
5.1	Results from operations . . . . .	40
5.1.1	Download time . . . . .	41
5.1.2	Grafana . . . . .	41
5.2	Results from calibration and analysis of Frohavet . . . . .	42
5.2.1	Radiometric and spectral calibration results . . . . .	42
5.2.2	Unsupervised classification results . . . . .	43
5.2.3	PCA results . . . . .	44
5.2.4	Unsupervised classification results of the masked and compressed Frohavet scene . . . . .	45
5.2.5	Radiance and reflectance of the masked Frohavet scene . . . . .	46
<b>6</b>	<b>Discussion</b>	<b>48</b>
6.1	Operations . . . . .	48
6.1.1	Mission planning, scheduling and downlinking data . . . . .	48
6.1.2	Monitoring correct scheduling . . . . .	49
6.1.3	Troubleshooting HYPSON-1 capture errors . . . . .	49
6.1.4	Requirements of operations . . . . .	49
6.2	Calibration and conversion . . . . .	52
6.2.1	Calibration . . . . .	52
6.2.2	Requirements of calibration . . . . .	53
6.2.3	Radiance to reflectance conversion . . . . .	53
6.2.4	Requirements of radiance to reflection conversion . . . . .	53
6.3	Analysis . . . . .	54
6.3.1	Unsupervised classification . . . . .	54
6.3.2	PCA . . . . .	55
6.3.3	Requirements of analysis . . . . .	55

---

---

6.4	Software used - STK, SNAP, and Excel . . . . .	56
6.4.1	Mission planning with STK . . . . .	56
6.4.2	SNAP . . . . .	57
6.4.3	Excel . . . . .	57
<b>7</b>	<b>Conclusion</b>	<b>58</b>
7.1	Findings . . . . .	58
7.2	Future work . . . . .	58
	<b>Bibliography</b>	<b>60</b>

---

# 1 Introduction

## 1.1 Motivation

The HYPSON-1 is a small research satellite developed at NTNU SmallSat Lab with a mission to scan lakes and oceans with a hyperspectral camera from about 500 km above the Earth to detect harmful algal blooms that can threaten ecosystems. HYPSON-1 is designed with a short orbital period and fast and reliable down-linking to ground stations. Thus, large quantities of data of oceanographic phenomena could be acquired to monitor climate change. However, a vast amount of requirements need to be satisfied in order for HYPSON-1 to reach its mission goals. This report focuses on evaluating how well HYPSON-1 satisfies these requirements. We want, in particular, to evaluate if satellite operations can meet operational needs. Furthermore, the data we collect should be tailored to end-users by extracting relevant spectral and spatial information in the water-leaving signals using, e.g., dimensionality reduction or classification [1]. Finally, operations will be evaluated to conclude any potential for improvement and if we will meet the satellite's five-year life expectancy. Operational errors that lead to, e.g., extra battery drain could potentially leave us without satellite communication way before this time. Will these requirements be possible to satisfy with today's resources, or does HYPSON need to invest more? If it succeeds, it will contribute to the revolutionary technology of small satellites, as traditional observation satellites take several years to develop and are much more expensive.

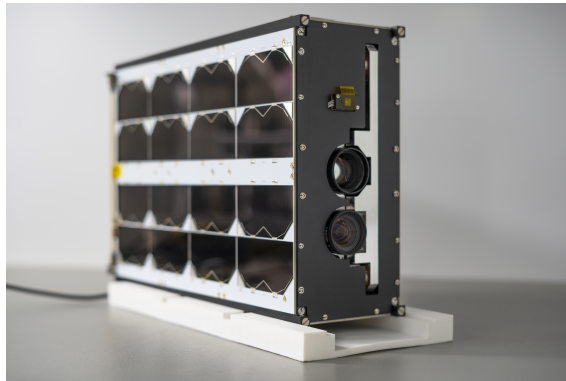


**Figure 1:** HYPSON-1 at NanoAvionics before launch [2].

## 1.2 Previous work

Hyperspectral remote sensing technology onboard spacecraft has significantly advanced in the past two decades [3]. Sensors with unprecedented spatial and spectral resolutions acquire data over large surfaces, resulting in better knowledge of the Earth. Previous work for the HYPSON team was written in the project thesis *Hyperspectral data analysis for chlorophyll estimation* by Fredrik Gran-Jansen [4]. The thesis described how wavelengths outside the visual spectrum appear when analyzing the spectral wavelengths of natural grass captured by an HSI, indicating the presence of chlorophyll-a. Applying an unsupervised machine learning algorithm to the data distinguished natural and artificial grass based on this spectral signature. The following experiment in [4] was to attach the HSI to a plane to acquire images over the ocean, thus, detecting chlorophyll-a concentration in algae. Operating on such aircraft was time-consuming and would only acquire images in small quantities and areas.

---

HYPSON-1 launched on the 13th of January 2022, attached with an HSI ensuring regular image acquisition over large areas, allowing us to analyze more data. One of the primary missions is to estimate chlorophyll-a concentration in Frohavet, Norway, as it is supported by robotic assets from NTNU's Mission Control Center, such as Autonomous Surface Vehicles (ASV), Autonomous Underwater Vehicles(AUV), and Unmanned Aerial Vehicles (UAV), deployed in Frohavet for in-situ observations [1].

We had contact with the satellite two weeks after launch, enabling us to test scripts made for image acquisition and data calibration and observe housekeeping telemetry. After several months of operations, acquiring and analyzing a vast amount of data, we finally captured an image over Frohavet with a desirable amount of cloud coverage, which will be the focus of this master's thesis.

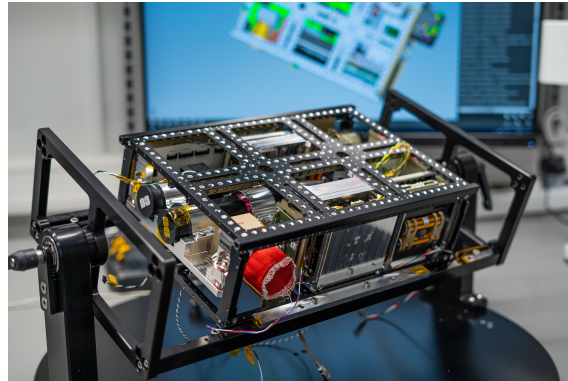


**Figure 2:** HYPSON-1 without its cover [2].

## 1.3 Thesis Objectives and Contributions

### 1.3.1 Thesis Objectives

HYPSON-1 got a major list of requirements in the spreadsheet "HYPSON-1 requirements" [5]. Some of these requirements will be focused on during this thesis and are displayed in the list below.

#### Operations

1. Shall enable flexible mission planning & scheduling and subsystem updates through successfully integrated up-linked mission data.
2. Spacecraft software & scheduling (including payload code) shall be open for updates (mission operations; change in objectives; bug fixes) and upgraded (functionality and efficiency) after launch.
3. Main Telemetry, Tracking and Command shall be sent and received through S-band.
4. S-band downlink shall be within the band 2,200-2,290 MHz with a bit rate of at least 800 Kbps.
5. S-band uplink shall be within the band 2,025-2,110 MHz.
6. The received data shall be logged to a file for archiving with timestamps.



- 
7. The software shall accept data for transmission from a buffer that is easily accessible for a user.
  8. Shall avoid imaging during complete cloud cover, excessive white caps and turbulent atmosphere.
  9. Level 1A (L1A) data product shall be downlinked in less than 24 hrs.
  10. L1A data shall have no more than 2200 frames and be less than 420 MB.
  11. Shall downlink house-keeping telemetry data for at least 1 pass per day.
  12. Target areas shall be less than 100x100 km<sup>2</sup> in Mid-Norway fjords/coast, Barents Sea, Greenland coast, Monterey Bay, and Svalbard fjords/coast and imaged between 06:00 AM and 13:00 PM Local Time in spring and summer season.
  13. Should be operational for at least 5 years with weekly mission updates.

### **Calibration**

14. Shall use radiometric and spectral calibration methods.

### **Analysis**

15. Collection of HSI frames shall be reconstructed into a datacube 3D image with at least 5 nm spectral resolution in the Visible–Near–Infrared (VIS-NIR) 400-800 nm spectral range.
16. Should take at least 1 image with less than 160 spectral bands in VIS-NIR with <10 nm spectral resolution.
17. Shall downlink 1 hyperspectral image in L1A data format containing detectable optical signatures (Chl-a, Colored dissolved organic matter (CDOM) etc.) to be processed on ground.
18. Operational data shall be useful for decision-making and in-situ validation with autonomous agents.
19. Should perform image acquisition of target areas where there is highest probability of detection off the coast of Norway with off-Nadir pointing capability.
20. To provide and support ocean color mapping through a Hyperspectral Imager (HSI) payload, autonomously processed data, and on-demand autonomous communications in a concert of robotic agents at the Norwegian coast.
21. Should enable atmospheric correction, dimensionality reduction, spectral compression, classification and target detection.
22. Solar zenith angle at target shall be less than 75 degrees.

### **Reflectance**

23. Digital values measured by the HSI on HYPSO-1 must be converted to Top of Atmosphere (ToA) reflectance. This is a custom made requirement for this thesis.

### **Georeferencing**

24. Be able to transform pixel indices to geodetic latitude and longitude, e.g., using georeferencing, such that the coordinates may guide in situ assets to specific locations of interest.

---

### 1.3.2 Thesis Contributions

The following contributions in the master's thesis are:

1. Evaluation of HYPPO's mission planning and image acquisition from the HYPPO-1 satellite.
2. Evaluation of HYPPO-1's life expectancy with focus on battery voltage.
3. Evaluation of available calibration methods and data conversions.
4. Analysis of HYPPO-1 data through dimensionality reduction and classification.
5. Analysis of optical signatures to detect chlorophyll-a concentration in HYPPO-1 data.
6. Investigated where HYPPO needs to put resources in order to satisfy its requirements.

### 1.4 Thesis Outline

Through this thesis, we will go step by step from planning a satellite capture mission to analyzing the calibrated HYPPO-1 data. Following this introductory section is an introduction chapter explaining hyperspectral remote sensing concepts, such as the Hyperspectral imager (HSI) design, ocean color, classification, principal component analysis, calibration, atmospheric correction, and radiance to reflectance conversion. The third Chapter presents the theory of operations, including HYPPO-1's concepts of operation (CONOPS), system, communication, and mission planning. Chapter four explains the methods used to meet the objective goals in two sub-chapters. The first contains detailed descriptions of mission planning and satellite operations before, during, and after a pass. The second processes the acquired calibrated hyperspectral data with unsupervised classification, dimensionality reduction, and radiance to reflection conversion. This section also creates a region of interest (ROI) over the ocean to reduce the amount of data. Chapter five provides the results from Chapter four, and the last-but-one Chapter discusses these results and determines whether or not the selected HYPPO-1 requirements are satisfied. The final Chapter summarizes the findings of the thesis and presents future work.

---

## 2 Theory of hyperspectral remote sensing

### 2.1 Overview of remote sensing

*Remote sensing* is the acquisition of data or information about an object or area from a distance, typically from satellite or aircraft [6]. It is often used to monitor ecosystems, forecast weather and temperature changes, manage ice, and observe ocean color. Remote sensing technologies can be categorized as either passive or active. The former is when a light source is used, while the latter is when light is actively sent from the sensor to strike a target [7]. This thesis focuses on imaging with a hyperspectral camera, a passive remote sensing technique.

### 2.2 Hyperspectral imaging

Reflection spectroscopy, a method of determining a target or area's spectral characteristics without coming into contact with the sample, is the foundation of the *hyperspectral imaging* approach [8]. Compared to a standardized optical camera that assigns each pixel the colors red, green, and blue (RGB), it analyzes a broader and more detailed spectrum of light. A hyperspectral image acquires more information about its target by separating the light in each pixel into many separate spectral bands [9].

Objects absorb and emit electromagnetic radiation in different ways creating unique spectra [10]. Hyperspectral imaging identifies these spectra and can therefore monitor agricultural health, food quality, and algal blooms. Such information can only be acquired beyond the visible spectra, thus, explaining the methods used for monitoring ecosystems by, for instance, obtaining data on chlorophyll from space [11].

### 2.3 Camera

#### 2.3.1 Design of the HSI

The hyperspectral imager on the HYPSONO-1 satellite is the *HSI*, a transmissive grating imager [12]. The small camera is assembled with simple components available on the market. The design is open-source and cost-efficient, making it possible for anyone to build hyperspectral imaging applications [13].

Wavelength bands are acquired as light spectra are dispersed through the HSI grating. Figure 3 shows the optical concept of the imager's design. First, the front lens  $L_0$  focuses incoming light on the slit  $S$  with height  $h$ . The narrow slit width  $W$  only permits a thin line of light through to the collimator lens  $L_1$ . Then the collimated light is separated through the transmissive grating  $G$ , much like a prism, before it strikes the detector lens  $L_2$  with refraction angle  $\beta$ . The light is then focused on the Complementary Metal-Oxide-Semiconductor (CMOS) detector  $D$  with length  $x$ , that converts photons into digital units. These raw measurements are later processed and calibrated by internal software to prepare for downlink. Each lens has an effective aperture  $D_n$  and focal length  $f_n$ .

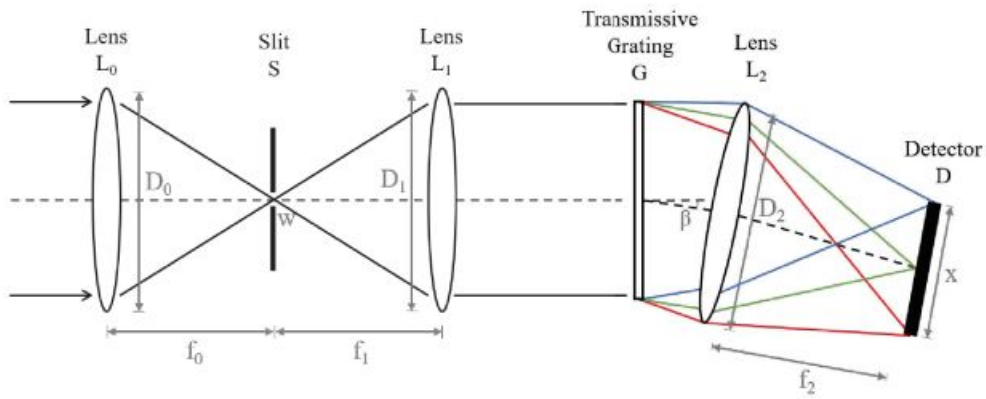


**Figure 3:** Illustration of the optical concept of a hyperspectral imager with transmissive grating, based on Eismann [14].

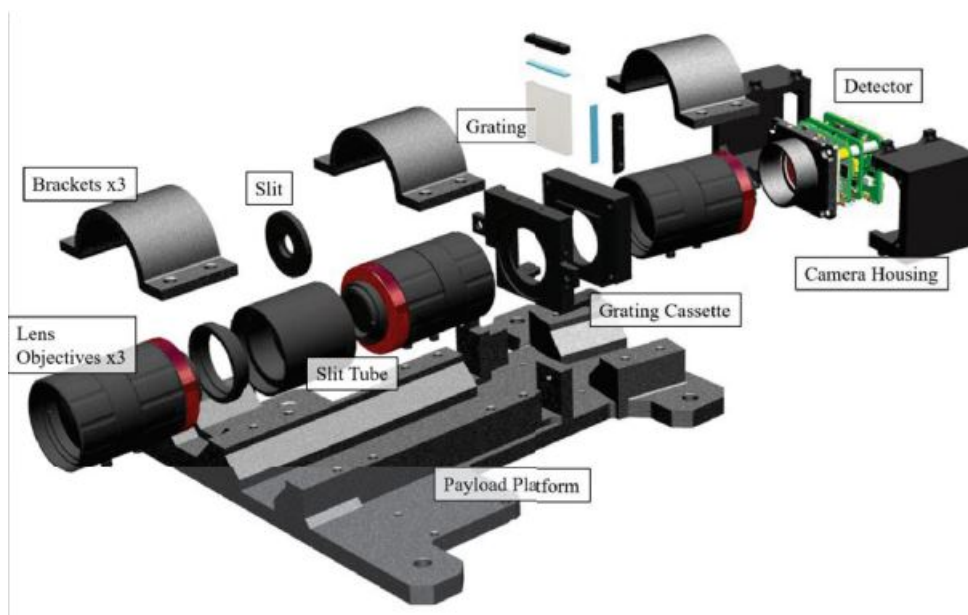


**Figure 4:** The design of the hyperspectral imager shown with components highlighted [12].

### 2.3.2 Pushbroom scanning

The HSI is a pushbroom scanner that records imagery by moving straight across the target area. The entrance slit is perpendicular to the direction of movement, as shown in Figure 5. Reflected light enters the slit and corresponds to a one-pixel row. Then the grating separates the light into different wavelengths, creating the spectrogram. The HSI creates a single hyperspectral image cube by combining the acquired pixel rows (Figure 6). The image is then described as a function of wavelength. The spatial resolution of the image is affected by the spacecraft attitude, the Field Of View (FOV), and the front optics [11].

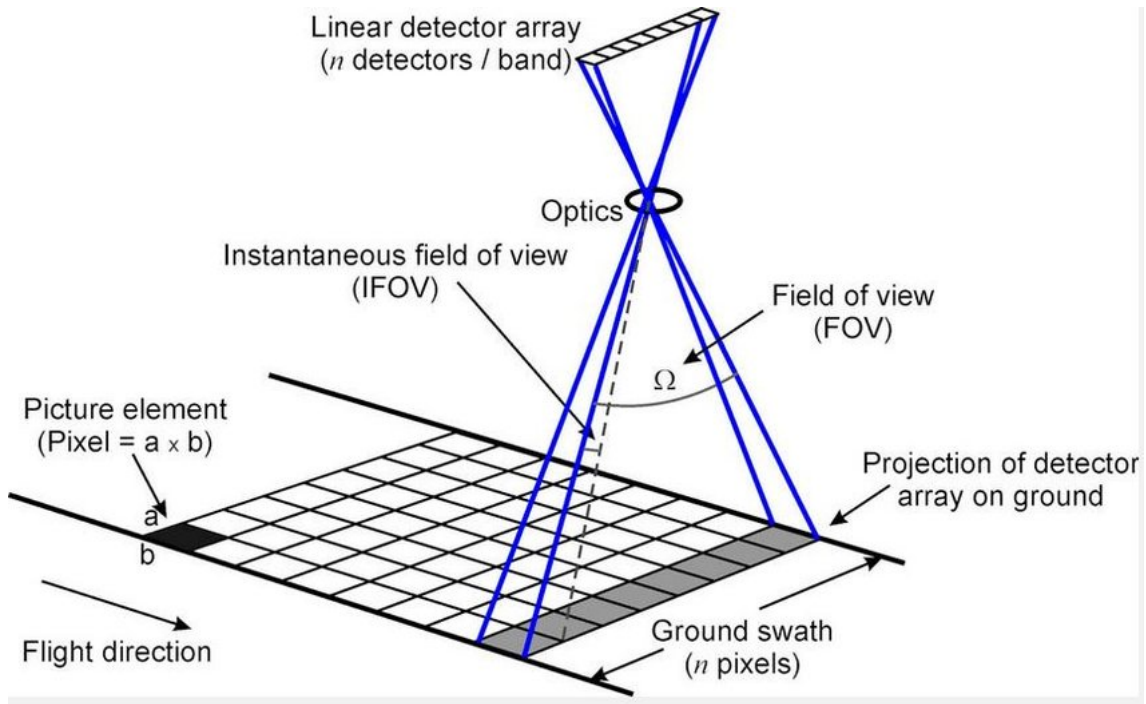


**Figure 5:** Principle of the pushbroom scanner [15]

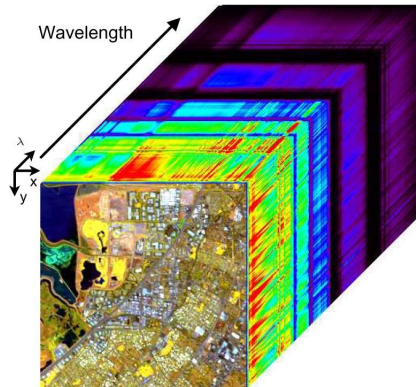


**Figure 6:** Hyperspectral cube. [16]

## 2.4 Ocean color

The ocean is one of the least studied ecosystems on Earth, but it also significantly impacts our climate. Because our climate is continually changing and varying, it is crucial to comprehend the ecology of our seas to secure a habitable world in the future. The subject of biological oceanography has been entirely transformed by Earth-orbiting spacecraft equipped with ocean color radiometry (OCR) [17]. OCR also contributes to ocean system modeling, fisheries oceanography, physical oceanography, and biogeochemistry. Additionally, the marine ecosystem cannot be observed at these scales without studying the ocean color.

The absorption and scattering of light give the ocean its signature blue color [18], as wavelengths between 445 nm and 520 nm are immediately reflected by the water molecules. Higher wavelengths are, on the contrary, absorbed. The scattering of light is increased by particles in the water that originate from various sources, such as the resuspension of

---

sand or biological material. Additionally, these particles can absorb specific wavelengths, creating unique spectral signatures.

#### 2.4.1 Why do we look for phytoplankton?

Most green plants in the water are microscopic single-celled organisms called phytoplankton that capture energy from the solar spectrum for photosynthesis. Chlorophyll in the phytoplankton scatters and absorbs this energy and, therefore, influences OCR as its spectral signature can be captured by spacecraft with radiometry instruments [17]. The acquired data can then be processed to visualize chlorophyll concentration, which gives an index of phytoplankton biomass. Figure 7 shows an image of harmful algal bloom captured by Landsat-8 [19].



**Figure 7:** Image of harmful algal bloom in Western Lake Erie from September 26, 2017. Captured by Landsat-8 [19]

#### 2.4.2 Chlorophyll-a

The reflectance of chlorophyll-a has distinctive spectral signatures between the wavelengths  $400\text{ nm}$  to  $800\text{ nm}$ , with peaks at  $465\text{ nm}$  and  $665\text{ nm}$  as shown in Figure 8 [20]. The cited experiment was conducted in a controlled environment with water containing various amounts of chlorophyll-a [21]. The different concentrations were examined and measured, confirming that increasing the concentration resulted in higher amounts of spectral reflectance.

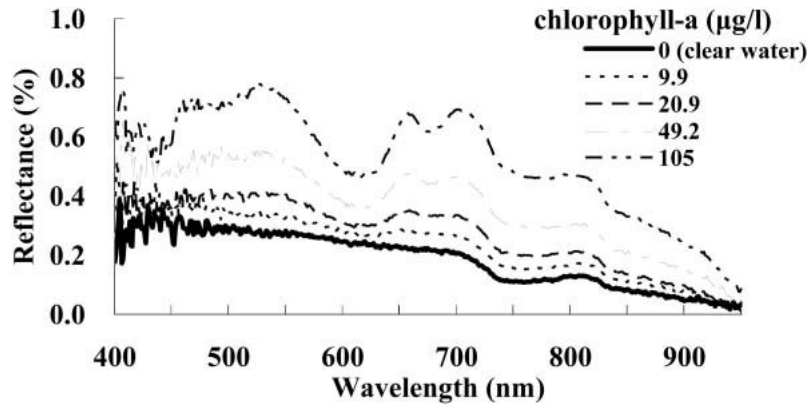


**Figure 8:** Measured spectral reflectance of clear water with different levels of chlorophyll-a concentrations [21].

## 2.5 Spectral calibration

### 2.5.1 Stray light

*Stray light* is light detected by an optical system that was not intended [22]. This light can originate from sources such as:

1. Unblocked or higher order diffraction peaks;
2. Scatter from screws and mirrors;
3. Unwanted reflections between imaging surfaces;
4. Emitted light from sensor elements due to high-temperature;

The latter can mainly produce stray light in infrared-sensitive systems, which is a problem for the HSI. This can result in the sensor detecting a higher amount of radiance and, thus, give incorrect spectral information.

### 2.5.2 Smile and keystone correction

Optical misalignments and aberrations can cause the accuracy of hyperspectral imaging sensors to degrade [23]. *Smile* and *Keystone* are features that distort the spectrum images and typically affect pushbroom imaging. The Smile effect causes center wavelength shift, while Keystone causes spatial band-to-band misregistration. Therefore, the acquired hyperspectral data has to be corrected for these distortions so that the accuracy of classification and other data processing techniques does not suffer. The features are presented in Figure 9.

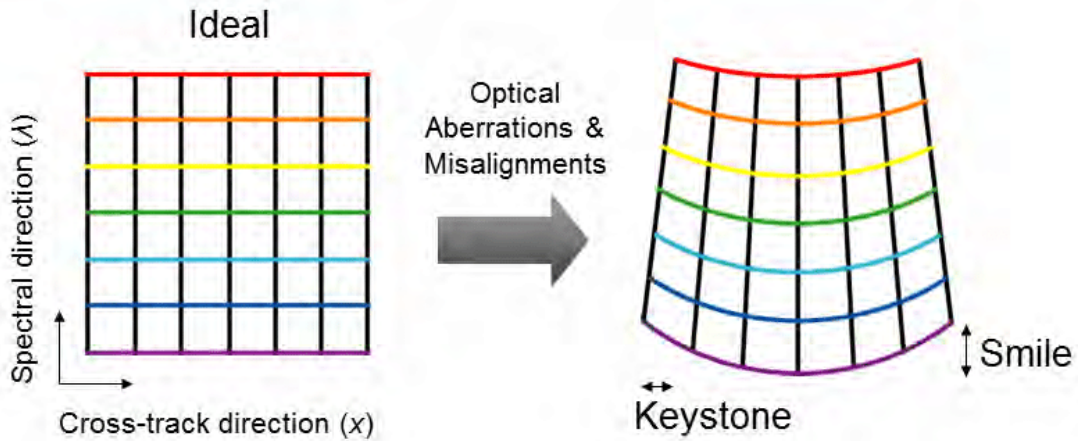


**Figure 9:** Smile and keystone distortions [23].

### 2.5.3 Atmospheric correction

*Atmospheric correction* is a technique that corrects for spectral signatures acquired when light passes through the atmosphere [24]. The light travels first through the atmosphere as solar irradiance, then as radiance back to the sensor. The atmosphere absorbs the energy, which reduces the electromagnetic intensity, resulting in a less accurate measurement from the sensor. This effect can, for instance, be shown as absorption lines in the measured spectra, such as the standard  $O_2$  absorption line. Additionally, inaccuracies in the reflectance spectra can be caused by scattering, which occurs when pixels affect their neighboring pixels with stray light. These two processes are the main contributors to atmospheric correction.

### 2.5.4 Calibrating a real camera

Spectral and radiometric calibration are the first steps toward analyzing the data captured by HYPSON-1. Spectral calibration matches each pixel with its corresponding wavelength to acquire correct spectral absorption peaks, and radiometric calibration converts pixel count to top of the atmosphere (ToA) radiance [25]. Pixel count is the intensity count that the sensor detects for each pixel.

Elizabeth Prentice guided a spectral calibration experiment during a lab session in the course TTK4265 - Optical remote sensing at NTNU [7]. This thesis presents this experiment as it gives an impression of how calibration is conducted.

A hyperspectral image was taken by the HSI of a white paper placed inside a closed cardboard box, with artificial fluorescent light striking the target. The spectrum of the light was known and is depicted in Figure 10.



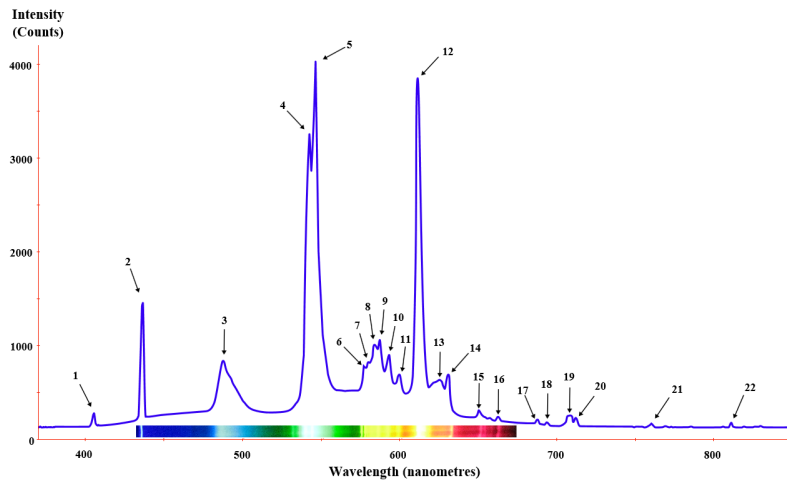


**Figure 10:** Spectrum of a typical fluorescent lamp [26].

The spectrum output of an arbitrary pixel was analyzed and compared to the spectrum output from the artificial lamp to convert pixels to nanometers. The result is depicted in Figure 11.

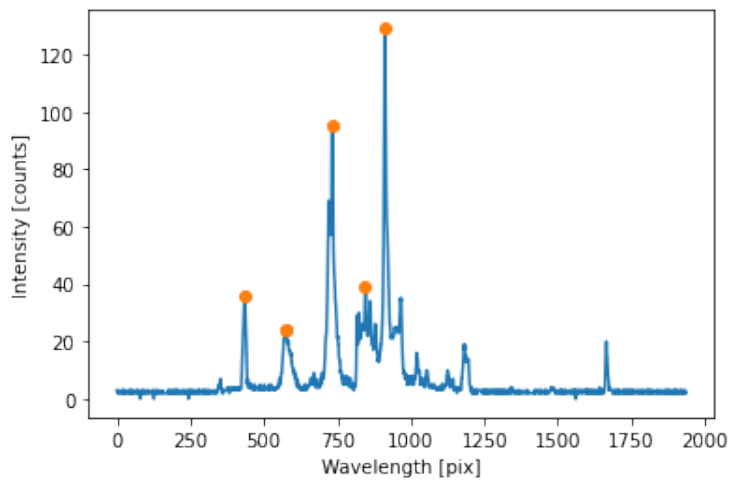


**Figure 11:** Spectrum of the image before calibration.

The most distinguishable peaks were highlighted with dots and were the ones to be compared to Figure 10. As the peaks were narrower and, thus, clearer, only the three pixels with the highest intensity were considered. Table 1 summarizes the result of the matching between pixels and nanometers.

Wavelength		Species
[ <i>pix</i> ]	[ <i>nm</i> ]	
434	435.8	Mercury
732	546.5	Mercury
912	611.6	Europium

**Table 1:** Coordinate matching of the three largest peaks between the spectra of the hyperspectral image and the fluorescent lamp.

Lastly, based on the matching, the rest of the pixels along the spectral dimension were converted to their respective wavelengths by applying a linear mapping to the raw data. Figure 12 shows the final calibrated picture.

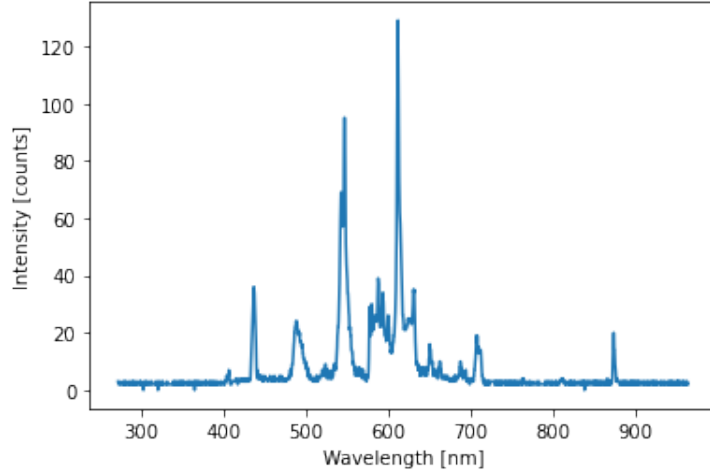


**Figure 12:** Calibrated spectrum of the image taken.

Using the above concept, a script made by HYPSO to calibrate the raw data was applied to the newly downlinked captures. This script also included radiometric calibration.

## 2.6 Classification of hyperspectral images

*Classification* is a data processing technique used to classify, for instance, hyperspectral images. The inputted pixels are clustered and mapped based on their spectral features. *Unsupervised classification* is a technique that inputs unlabeled pixels with a specified number of clusters as output. This is necessary when analyzing an area with spectral features that are not visible to the naked eye. Furthermore, collecting ground truth information simultaneously across an entire ocean scene is not feasible, thus, clustering is an important technique when searching for chlorophyll-a in the ocean.

### 2.6.1 K-means algorithm

*K-means* is a unsupervised classification algorithm commonly used to analyze hyperspectral data [14]. It is based on the following equation that minimizes the mean-squared error (MSE):

$$MSE = \frac{1}{N} \sum_{k=1}^K \sum_{\mathbf{x}_i \in \omega_k} (\mathbf{x}_i - \boldsymbol{\mu}_k)^T (\mathbf{x}_i - \boldsymbol{\mu}_k) \quad (1)$$

where  $\boldsymbol{\mu}$  is the mean vector,  $\mathbf{x}$  is the feature vector, and  $\omega_k$  is the clusters with  $N$  number of samples.

Based on the inputted class sample statistics, k-means iteratively estimates each vector class's mean. Additionally, based on the nearest mean classification,  $K$  clusters are generated by partitioning the data sets such that each pixel only belongs to one cluster.

---

Micheal T. Eismann presents six steps in his book *Hyperspectral Remote Sensing* that show how to apply k-means clustering [14]. These steps are listed below:

1. "Define the number of classes  $K$  to represent the data."
2. "Set the initial class mean vectors  $\boldsymbol{\mu}_k$  from either *a priori* data or by randomly selecting  $K$  image spectra or feature vectors."
3. "For each image spectrum or feature vector  $\boldsymbol{x}_i$ , compute the Euclidean distance  $d_k$  in Eq. 2, for each class means vector, and assign the sample to class  $\omega_k$  with minimal distance."
4. "After all samples have been assigned, update the mean vector for each class to the sample mean of all spectra assigned to the class."
5. "Determine the amount of change in terms of either the number of spectra that switched classes or the average shift in class mean vectors."
6. "Repeat steps 3, 4, and 5 until convergence based on the change is appreciably small."

$$d_k = \|\boldsymbol{x}_i - \boldsymbol{\mu}_k\| \quad (2)$$

## 2.7 PCA

A downside of using classification on a hyperspectral image to study the ocean characteristics is the vast data set that hyperspectral data contains. As HYPSO-1 has close to 3.5 *nm* spectral width between neighboring bands, optical signatures of pertinent physical phenomena are often present across many bands. Thus, the information becomes redundant. As each band conveys redundancy, processing complexity and time increases without increasing the accuracy or value of the analysis [27]. The classification quality may also decrease as more bands are used as input. Therefore, it is often necessary to perform preprocessing to effectively reduce the hyperspectral data set or select the most relevant bands for the required analysis. *Principal Component Analysis* (PCA) is a preprocessing technique that reduces data size by creating new bands containing the most significant spectral information. Further in this thesis, we will:

1. Apply PCA to the hyperspectral data to reduce the dimensionality used for classification;
2. Use PCA to determine what bands to use;
3. Apply the k-means classification algorithm to a HYPSO-1 data set, with and without dimensionality reduction with PCA;
4. Evaluate the results to determine the applicability of PCA on hyperspectral data.

To explain what PCA is, we follow below the discussion from the article *Principal Component Analysis for Hyperspectral Image Classification* written by Craig Rodarmel and Jie Shan [27].

PCA transforms the hyperspectral data to remove the correlation among the bands and examine band dependency. The procedure determines the optimal linear combination of

the original bands by accounting for pixel value variance in an image. This is done by analyzing the decomposed eigenvalues of the covariance matrix of the hyperspectral image bands.

An image pixel vector  $\mathbf{x}_i$  is defined as:

$$\mathbf{x}_i = [x_1, x_2, \dots, x_N]_i^T \quad (3)$$

where, as seen in Figure 13,  $x_1, x_2, \dots, x_N$  is the pixel values at one corresponding pixel location for each  $N$  hyperspectral bands of the hyperspectral image data.

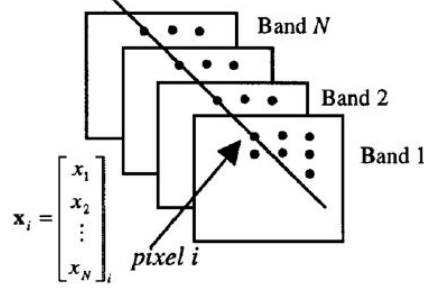


**Figure 13:** Pixel vector  $\mathbf{x}_i$  from PCA [27].

The mean vector is defined as:

$$\mathbf{m} = \frac{1}{M} \sum_{i=1}^M [x_1 x_2 \dots x_N]_i^T \quad (4)$$

where  $M = m * n$  is the number of image pixel vectors defined by the hyperspectral image with  $m$  rows and  $n$  columns, and  $i = (1, 2, \dots, M)$ .

The next step is to calculate the covariance matrix of  $\mathbf{x}$ , which is defined as

$$\mathbf{Cov}(\mathbf{x}) = \mathbf{E}(\mathbf{x} - \mathbf{E}(\mathbf{x}))(\mathbf{x} - \mathbf{E}(\mathbf{x}))^T \quad (5)$$

where  $\mathbf{Cov}$  is the notation for the covariance matrix and  $\mathbf{E}$  is the expectation operator.

The covariance matrix can be approximated by the following equation:

$$\mathbf{C}_x = \frac{1}{M} \sum_{i=1}^M (\mathbf{x}_i - \mathbf{m})(\mathbf{x}_i - \mathbf{m})^T \quad (6)$$

The PCA is based on the covariance matrix's eigenvalue decomposition as follows:

$$\mathbf{C}_x = \mathbf{A} \mathbf{D} \mathbf{A}^T \quad (7)$$

where  $\mathbf{A}$  is the orthonormal matrix composed of the eigenvectors  $\mathbf{a}_k$  ( $k = 1, 2, \dots, N$ ) of  $\mathbf{C}_x$  as such:

---


$$\mathbf{A} = (\mathbf{a}_1, \mathbf{a}_2, \dots, \mathbf{a}_N) \quad (8)$$

and  $D$  is the diagonal matrix:

$$\mathbf{D} = \text{diag}(\lambda_1, \lambda_2, \dots, \lambda_N) \quad (9)$$

with the covariance matrix's eigenvalues  $\lambda_1, \lambda_2, \dots, \lambda_N$ .

The next step is to do a linear transformation as follows:

$$\mathbf{y}_i = \mathbf{A}^T \mathbf{x}_i \quad (10)$$

for  $i = (1, 2, \dots, M)$ . This computes the PCA pixel vectors which form the transformed PCA bands of the initial images.

The eigenvectors and eigenvalues are arranged in descending order such that  $\lambda_1 \geq \lambda_2 \geq \dots \geq \lambda_N$  so that the first  $K$  eigenvectors  $\mathbf{a}_j^T$  ( $j = 1, 2, \dots, K$ ) of matrix  $\mathbf{A}^T$ , where  $K \ll N$ , is used for the approximation calculation of the original images. This is defined by the following:

$$\mathbf{z}_i = \begin{bmatrix} z_1 \\ z_2 \\ \vdots \\ z_K \end{bmatrix}_i = \begin{bmatrix} a_{11} & a_{12} & \dots & a_{1K} & \dots & a_{1N} \\ a_{21} & a_{22} & \dots & a_{2K} & \dots & a_{2N} \\ \vdots & \vdots & \vdots & \vdots & \vdots & \vdots \\ a_{K1} & a_{K2} & \dots & a_{KK} & \dots & a_{KN} \end{bmatrix} \cdot \begin{bmatrix} x_1 \\ x_2 \\ \vdots \\ x_K \\ \vdots \\ x_N \end{bmatrix}_i \quad (11)$$

for  $i = (1, 2, \dots, M)$ , where  $\mathbf{z}_i$  is the pixel vector of the first  $K$  bands of the PCA images.

As we have the eigenvectors and eigenvalues in descending order, we ensure that the highest variance or contrast is in the first bands, and the lowest variance or contrast is in the last bands. Most of the information in correlation with the original hyperspectral image is contained within the first  $K$  PCA bands. The advantage gained is that both image noise and total bands are reduced, giving a more effective and accurate analysis going forward. Furthermore, PCA bands are mutually independent with the covariance matrix defined as:

$$\mathbf{C}_z = \text{diag}(\lambda_1, \lambda_2, \dots, \lambda_K) \quad (12)$$

## 2.8 Radiance to reflectance

The digital values measured by the HSI on HYPSONO-1 must be converted to Top of Atmosphere (ToA) reflectance to be correctly analyzed. First, the values are converted to ToA spectral radiance after calibration. *Spectral radiance* is defined as radiance emitted or reflected off a surface per unit wavelength, with units watt per steradian per square meter per nanometer  $mW/(m^2 nm sr)$  [28]. It indicates how much a remote sensing instrument directly measures at its given angle of observation. *Steradian* is defined as a dimensionless SI unit of a solid angle [29].

*ToA reflectance* is the percentage of radiation striking a target compared to the reflected radiation, measured at the top of Earth's atmosphere [30]. It includes contributions from atmospheric effects, clouds, and gasses and therefore has to be compensated with atmospheric correction. To convert ToA radiance (LTOA) to ToA reflectance (RTOA), the following equation expressed by Sentinel Application Platform from ESA, can be done:

$$R_{TOA}(\lambda) = \frac{\pi L_{TOA}(\lambda)}{E_0(\lambda)\cos(\theta)} \quad (13)$$

where  $E_0$  is the the solar spectral irradiance and  $\theta$  is the solar zenith angle measured in radians.

### 2.8.1 Solar zenith angle

The *solar zenith angle* is defined as the angle between the vertical direction, and the angle from that point to the sun [31]. The solar zenith angle depends on the local date and time and the position on Earth. From Figure 14 it can be determined that the higher the sun is relative to the observed location, the lower the solar zenith angle is.

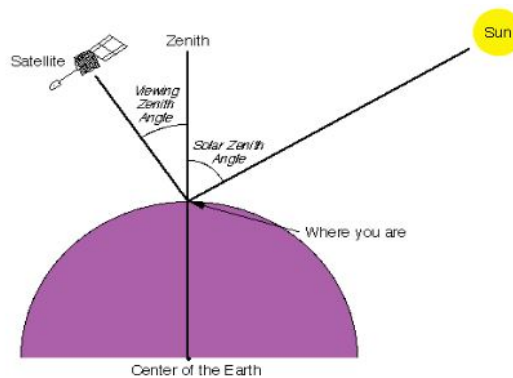


**Figure 14:** Solar Zenith Angle [32]

---

## 3 Theory of operations

To evaluate whether or not the requirements of the HYPSON-1 mission are met, we need to look at the software and hardware used to operate the satellite. This section covers fundamental theories of each subsystem used during the stages of operations. These stages are introduced as concepts of operations (CONOPS), illustrating the five significant events during HYPSON-1's missions.

### 3.1 CONOPS

The HYPSON-1 satellite has an altitude of 500 km with a sun-synchronous orbit and a local time of descending node at 10:00 AM. This orbit ensures daytime access to observe the Norwegian coastline as well as avoiding detrimental sun-glint effects [33]. HYPSON-1's overall mission utility and performance are primarily determined by spectral and spatial resolution trade-offs, signal-to-noise ratio, observation locations, coverage to ground stations, latency, and data size. Figure 15 shows the five steps for the HYPSON-1 CONOPS as presented in *"Development of a Small Satellite with a Hyperspectral Imaging Payload and Onboard Processing for Ocean Color"* by Sivert Bakken [33]:

1. "After receiving telecommands and updates (e.g camera settings) that are uploaded from a nearby ground station, HYPSON-1 is scheduled to orient its hyperspectral imager to start scanning a pre-defined area size;"
2. Acquires hyperspectral images for a short duration under either off-nadir pointing or slew maneuver;
3. "After imaging, the hyperspectral images are processed onboard immediately to reduce their data size and to speed up the download to the ground;"
4. "For quick downlink after observing coastal regions in Norway, the selected ground station network includes S-band ground stations at NTNU Trondheim, KSAT Svalbard, Norway and KSAT Puertollano, Spain;"
5. "In addition, the Mission Control Center at NTNU operates several supporting robotic agents, such as UAVs, ASVs and AUVs, that may collect in-situ data if within range of the observed area;"

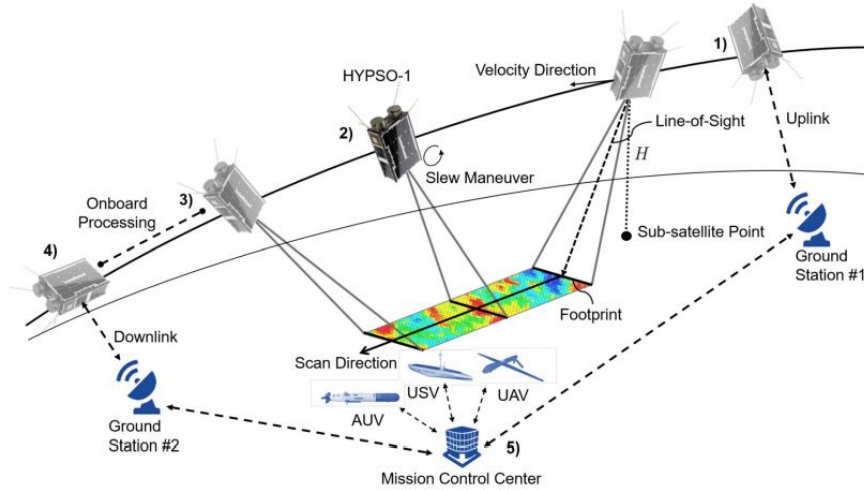


**Figure 15:** Illustration of CONOPS [33]. 1) Configurations from a nearby ground station are uplinked to HYPSONO-1; 2) acquires hyperspectral images for a short duration under either off-nadir pointing or slew maneuver; 3) processes images onboard; 4) nearby ground stations receive downlinked data; and 5) the observed scene is measured with in-situ assets for closer investigation. Illustration provided by Mariusz E. Grøtte in [1].

## 3.2 HYPSONO-1 system

To fulfill the mission CONOPS and user needs, the satellite’s architecture needs to contain several pieces of hardware, as illustrated in Figure 16. As we operate on a majority of these instruments daily, it is necessary to explain their usage.

### 3.2.1 Satellite Bus

The following section is based on the paper *Ocean Color Hyperspectral Remote Sensing with High Resolution and Low Latency – the HYPSONO-1 CubeSat Mission* that describes the satellite bus and its components [1]. The spacecraft bus provided by NanoAvionics was chosen to accommodate the hyperspectral imager (Figure 16). The components of the bus are, among others the Payload Controller (PC), which serves as a storage device and router between the satellite bus and payload, the Electrical Power System (EPS), the Ultra-High-Frequency (UHF) radio, and the Flight Computer (FC), which handles attitude determination and control system (ADCS) functions and onboard data handling. Also, the CubeSat Space Protocol (CSP) is used for internal communication on the spacecraft through a Controller Area Network (CAN). Each subsystem is a network node with a specific CSP address.

HYPSONO-1 is further equipped with:

1. A *Star Tracker* and *Inertial Measurement Unit (IMU)* for accurate attitude determination during imaging. Before imaging, the sensors are switched on for at least five minutes to ensure adequate settling time. When no images will be captured, three gyroscopes, three magnetometers, and six sun sensors will be employed, which will return coarser attitude information but use less power;
2. Four *reaction wheels* for attitude control, three of which are orthogonally positioned



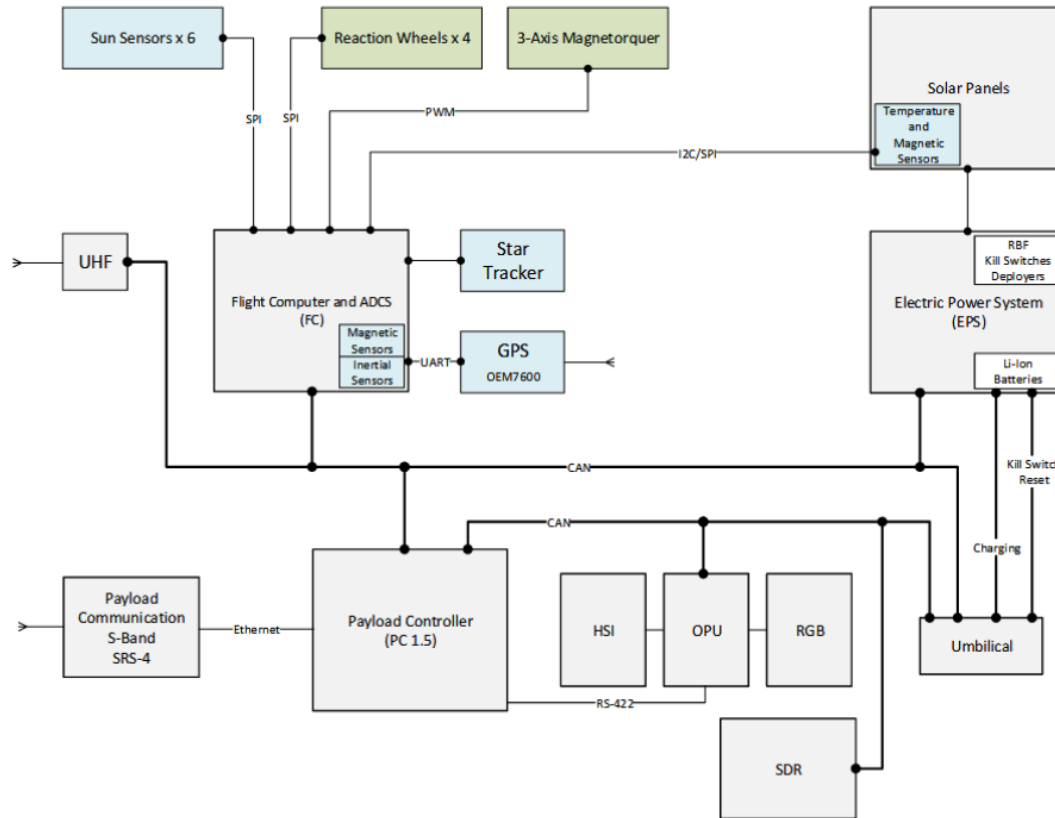


Figure 16: HYPSO-1 Architecture [34]

along the body axis, and the fourth is inclined at an angle of  $54.7^\circ$ . Each of these wheels has a maximum torque of 3.2 mNm. Two magnetorquers are positioned along each body axis to dump the momentum of the reaction wheels.

3. A 2.4 GHz *S-band* Transceiver with a data rate of 1 Mbps for downlinking payload data;
4. An *Onboard Processing Unit* (OPU), allowing in-orbit software updates and 8 GB storage capabilities. Small amounts of data can be downlinked directly from the OPU, while more significant amounts of data must be buffered from the OPU to the PC over CAN before it is downlinked over the S-band radio. By buffering data to the PC, one enables full utilization of the S-band data rate and allows the OPU to be turned off faster.

### 3.2.2 Attitude Determination and Control System

An *ADCS* is required to achieve a spatial resolution better than 100 meters [1]. During image acquisition, the satellite is pointing and maneuvering, causing attitude sensor noise and actuator inaccuracies, such as jittering of a reacting wheel. This can cause non-uniform distribution of the acquired images. The ADCS ensures that the satellite is stable and that the pointing is correct. Consistent image registration where each pixel's location on the observed scene is known, with an accuracy of 100 m, is defined as geo-referencing. This requires high performance of orbit position accuracy, attitude knowledge accuracy, and time synchronization between the attitude data and captured images. The ADCS

---

involves instruments such as magnetorquers, star trackers, reaction wheels, and sun-sensors connected to the rest of the payload.

The different components are described as such:

1. The *magnetorquers* enable microsatellite attitude control with the use of electromagnetic coils [35]. The magnetorquer interfaces with Earth's ambient magnetic field, creating a magnetic dipole that produces proper torque in the form of counter-forces.
2. *Star trackers* measure the line-of-sight vector to astronomical objects visible to the sensor [36]. These sensors memorize a map of a particular region of the cosmos and compare it to the star constellation visible via the sensor's field of view. Thus, the star tracker acquires accurate and autonomous attitudes.
3. The *reaction wheels* are used on HYPSON-1 for three-axis attitude control [37]. The benefit of reaction wheels is that they provide a high pointing accuracy, ensuring that the satellite rotates by only small amounts. Such is crucial when the hyperspectral camera observes a specific location on Earth.
4. The *magnetometer* is used for attitude knowledge while images are not being taken, as it consumes less power from the EPS [38]. As Earth's magnetic field varies depending on the interaction between the Earth's magnetosphere and charged particles from the sun, magnetometers measure the intensity, strength, and direction, leading to attitude determination.
5. Similar to the magnetometers, the *sun sensors* are also used for attitude determination while images are not being taken [39]. This is also due to the sensors requiring low amounts of power from the EPS. The sun sensor determines the attitude by detecting the position and direction of the sun relative to the satellite. The detection is done by photosensitive units lying on the top of the sensor device, measuring the angle of incidence by converting striking photons to electric currents.

### 3.2.3 EPS

HYPSON-1's status must be examined regularly to ensure no problems arise in any subsystems during its orbital activities. The *Electrical Power System's* (EPS) primary function is to provide the necessary electrical power for other satellite systems to operate effectively [40]. The EPS's power source is energy gathered by solar panels exposed to direct solar radiation. Batteries store the energy that can be used when the satellite regularly passes through Earth's shadow. Batteries can also assist in supplying enough power to the satellite's payload during periods of high demand. The EPS must then distribute the acquired and stored power to other systems within the satellite as needed. The EPS also manages different voltage levels required by subsystems and sensors.

Another core function is to collect routine data from numerous subsystems and sensors called *housekeeping* telemetries [40]. This involves taking measurements of various temperatures, currents, and voltages. These are transmitted to the ground as part of the satellite's telemetry, allowing operators to monitor the overall health of their system and avoid any problems or poor performance.

---

### 3.2.4 Payload Controller (PC) and Flight Computer (FC)

The *PC* is a component supplied by NanoAvionics used to control the CLAW-1 payload [41]. *CLAW-1* is used to observe and capture images of algae growth using a RGB camera and an HSI. Target capture scripts made on the ground are uploaded to the PC, which communicates the commands to CLAW-1. Feedback from the payload to the PC is not possible, thus, all commands have to be manually timed and given a delay before the next command is issued. The *FC* controls the satellite's ADCS and is responsible for HYPSON-1's pointing during a capture, which is essential for imaging the correct scene.

## 3.3 Communication

This section describes the steps and terms used for communicating with HYPSON-1. This is done to get a grasp of how we are doing things now, and what can potentially be improved. The first step is to deliver generated scripts to HYPSON-1 through up-linked configurations from a nearby ground station.

### 3.3.1 NanoMCS and hypso-cli

To communicate with HYPSON-1, we can use two *command-line interfaces* (CLI) [42]. The first is *nanoMCS*, developed by NanoAvionics and used to operate on the satellite subsystems, e.g., uploading files to the PC and FC. It gives live and direct access to the satellite. The second is *hypso-cli*, developed by NTNU and used to communicate with the OPU on the payload.

### 3.3.2 Generating PC and FC scripts

The PC and FC cannot interpret CLI-commands written in ASCII, so the code has to be converted to hex-code within the CSP packets [41]. The command used for csp hex-codes is *csp txrx* with the following arguments: *csp txrx* <csp ID> <port> <Timeout (wait for ack) (ms)> <hex-code>. Translation of CLI-commands to hex-codes are done by using a *-p* flag, which is done by the following command to open the hypso-cli:

```
rlwrap ./hypso-cli 14 -p -ccan0=0/0.
```

A hypso-cli log file with hex-codes is generated with all the commands from the terminal using a log-parser python-script. These commands are parsed and translated to *csp txrx* commands.

### 3.3.3 Up-link and down-link through the S-band

HYPSON-1's S-band transceiver is the full-duplex Satlab SRS-4 designed for microsatellites with high-speed data transfer [43]. Full-duplex indicates that the signal carrier receives and delivers data transmission simultaneously. It enables integration with independent ground station networks, with a transmitter frequency of 2200 to 2290 *MHz* and a receiver frequency of 2025 to 2110 *MHz*.

---

## 3.4 Mission planning

The uploaded PC and FC scripts need correct timing and quaternions to ensure precise captures. Thus we need to acquire the exact location of the satellite relative to the area of interest during capture, alongside its Unix time. Also, higher satellite elevation provides a better camera angle, reducing atmospheric effects and increasing the quality of the captured image. *Elevation* is referred to as the angle between the observer's local horizon and the satellite [44]. This angle is between 0° and 90° for visible objects.

For mission planning, we are using Systems Tool Kit (STK) made by Ansys Government Initiatives to acquire the correct time, elevation, position, and velocity of the satellite relative to the target location. STK is a digital mission engineering platform allowing users to examine actual time capture missions [45]. HYPSON-1's orbit is tracked and can be modeled in a three-dimensional simulation, ensuring that the variables listed above are easily accessible. Then, a Matlab script created by HYPSON calculates the correct quaternions.

### 3.4.1 Timing - PC/FC scripting

Timestamps are essential in the scripts as they inform the satellite of when to do specific actions [41]. For instance, the FC script turns on the star tracker 30 minutes ahead of the capture script to get the satellite's correct position. Also, delays in booting up the OPU and the HSI, as well as script command delays, require the capture script to be initialized a predefined number of seconds before the start of capture. Lastly, a 40 minutes timestamp is set for the OPU to shut down to ensure enough time for buffering the capture file.

Timestamps are also made internally in the PC and FC script, as the PC cannot wait more than three seconds for an acknowledgment. The delay is defined in the number of milliseconds the PC has to wait before executing the next command line. The script delay command is defined as:

```
script delay <timeout in ms>
```

For script delays higher than 600000 ms (10 minutes), issuing a command that tells the PC to wait until a specific Unix time before executing the following line is needed. That can be done with the following command:

```
script delayuntil <unix_timestamp_in_seconds>
```

The last type of delay that needs to be considered when timing a capture deals with commands that cause timeout errors. These commands wait for a set amount of milliseconds before running the following line.

All timestamps are in the form of Unix timestamps which are acquired from the website *EpochConverter.com*, by manually typing in the date and time.

### 3.4.2 Quaternions

Correct orientation of HYPSON-1's attitude in space is crucial to ensure consistent operations and captures. We use quaternions to represent the attitude parameters, as they are computationally less intense and have no singularities compared to other attitude parameters such as Euler angles [46].

A quaternion can be thought of as a vector with four components describing how a frame, e.g., the body frame, is in relation to another frame, e.g., the LVLH frame. The coordinate axes  $(\hat{x}_o, \hat{y}_o, \hat{z}_o)$  of the LVLH frame point towards the velocity vector, the normal to the orbital plane, and the Earth's center, respectively [47]. The origin  $\mathcal{O}_o$  is placed on the satellite center of mass. The body frame has its axes  $(\hat{x}_b, \hat{y}_b, \hat{z}_b)$  pointed towards the principal axes of inertia, with the origin  $\mathcal{O}_b$  at HYPSON's center of mass.  $\hat{y}_b$  points through the axes of the largest principal inertia, and  $\hat{z}_b$  points through the smallest.

Figure 17 shows an illustration of HYPSON-1 in orbit [47], with the following frames: The body Frame  $\mathcal{F}_b$ , a desired Frame  $\mathcal{F}_d : \{\mathcal{O}_b, \hat{x}_d, \hat{y}_d, \hat{z}_d\}$  with arbitrary axes and origin in HYPSON's center of mass, and the Earth-Centered-Inertial (ECI) Frame  $\mathcal{F}_i : \{\mathcal{O}_i, \hat{x}_i, \hat{y}_i, \hat{z}_i\}$  located at Earth's center of mass.  $r_{ib}$  is the spacecraft inertial position, and  $v_{ib}$  is the spacecraft inertial velocity.

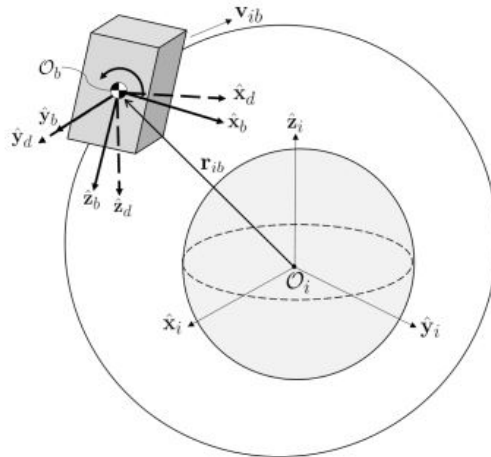


**Figure 17:** Illustration of HYPSON-1 in orbit with its defined ECI frame, body frame, and desired frame [47].

The ADCS subsystem takes the quaternion to make HYPSON-1 take the desired orientation. The ADCS then performs attitude control actions to align HYPSON-1's body frame axes with the given desired frame axes specified by the quaternion. Thus, the HSI will point along the z-axis in the direction of interest.

---

## 4 Experimental setup

The aims of this chapter are twofold: First, we prepare a mission and operate on HYPSO-1 to acquire the data and check the satellite's health. Second, we calibrate the data to obtain correct spectral and radiometric values and analyze it with data processing methods to classify the ocean. The ultimate goal is to evaluate how well the process of acquiring and analyzing a hyperspectral image captured by HYPSO-1 is.

### 4.1 Order of operations

In this chapter we present the process used to plan and execute a data acquisition with HYPSO-1. We aim to validate the Objectives 1-13 under "Operations" and Objective 24 under "Georeferencing".

#### 4.1.1 Preparations for observing a scene

To prepare for a capture, the following factors had to be considered:

1. The satellite maximum elevation relative to the observation area;
2. Weather such as the amount of sunlight and cloud coverage;
3. Potential algae concentrations;
4. In-situ data collected by robotic agents from the Mission Control Centers, such as UAVs, ASVs and AUVs;
5. The time interval between the last and next capture, to ensure that two captures did not overlap.

As these factors shifted weekly, we planned the captures regularly to ensure we had the most updated information.

For instance, an excellent area for HYPSO-1 to acquire hyperspectral images are over a lake or the ocean where the weather is clear, there is known algae concentration in the water that can be compared with the local Mission Control Center, and the elevation of the satellite is near zenith. As the orbit of HYPSO-1 is known, water bodies such as Lake Balaton, Puerto Montt, and Frohavet will always have good elevation during the day. This qualifies them to be primary areas of interest as there have also been observed high amounts of algae concentration in the waters.

The next step after mission planning is to acquire the satellite's time, position, and velocity variables as it reaches maximum elevation over the observation area.

#### 4.1.2 Target capture planning with STK

In this section, we present the process of mission planning to validate how well it meets the requirements of Objective 1.

---

STK is a tool for target capture planning as it tracks the orbit of satellites such as HYPSON-1. First, STK is opened to create a new scenario with an analysis interval. The interval was determined by which days we wanted to acquire information. Then the HYPSON-1 satellite was found from STK's standard object database. The next step was to insert a new place with the longitude and latitude for the location of interest. The place was also created with a constraint in elevation, set to be a minimum of 40 degrees. This is due to a lower angle being less preferable as it would result in a worse image due to atmospheric effects.

With the satellite and place inserted in STK's Object Browser, a 3D and 2D Graphic of Earth were displayed with the current orbit of the satellite and the specified location of interest in Figure 18.

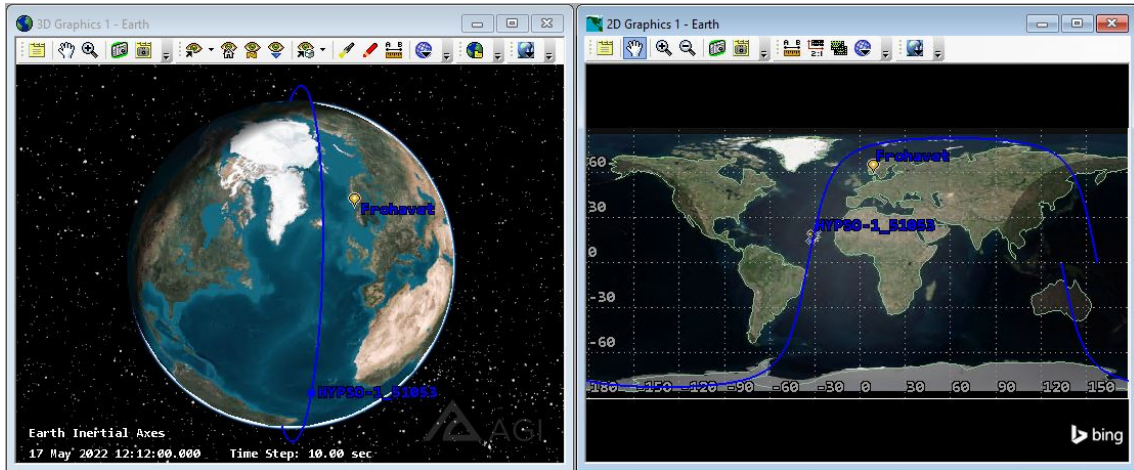


Figure 18: 3D and 2D image of the HYPSON-1 orbit and the observation area.

The next step was to create an access report within the scenario period. This report returns the azimuth, elevation, and range (AER) between two objects as seen in Figure 19. We focus on the maximum elevation and the time, as the closer to zenith, the better the image. The time ensures that we are only looking at passes during which there is still radiance from the sun striking the location. The time for maximum elevation during a day is inputted in the STK time display, as seen in Figure 20.

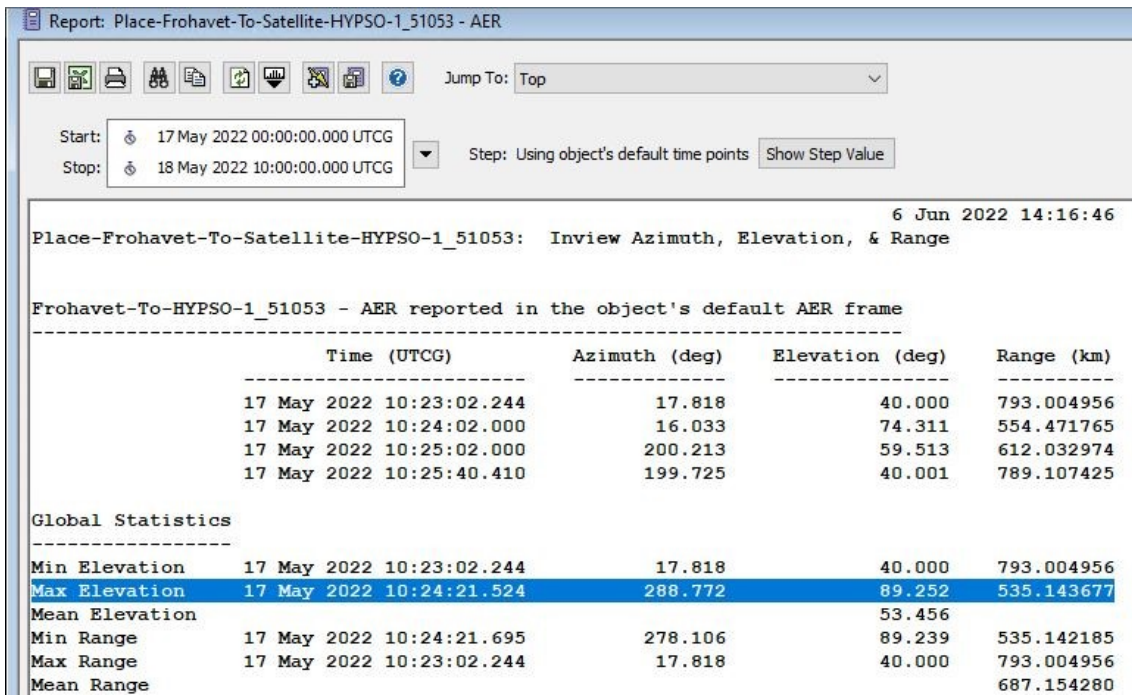


Figure 19: Access report which shows times and elevation of potential imaging opportunities.

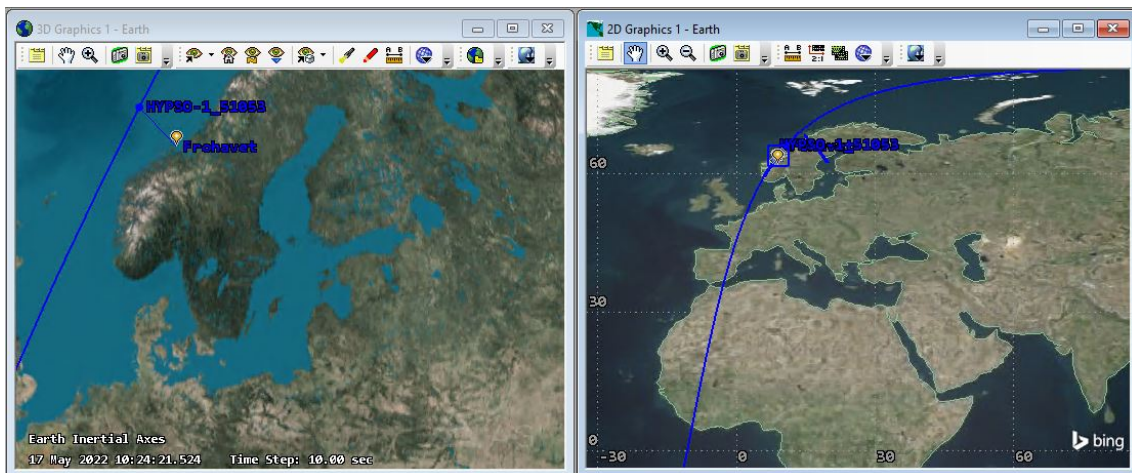
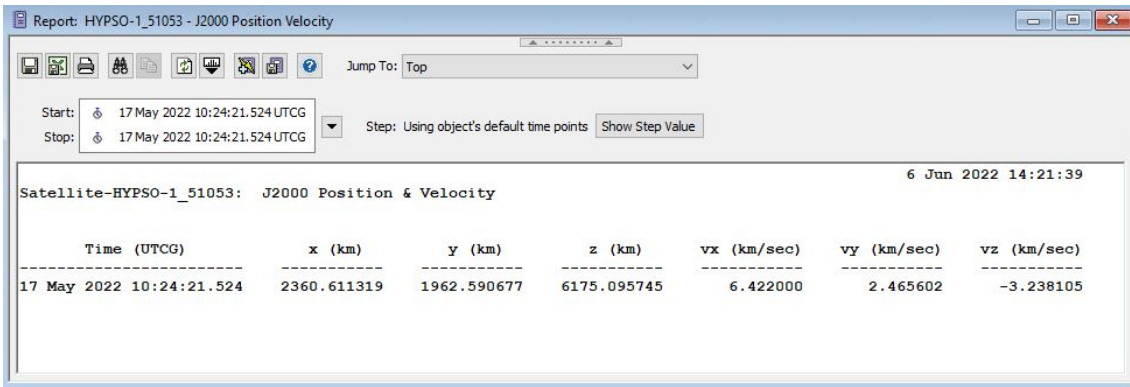


Figure 20: 3D and 2D image of the HYPSO-1 orbit and the observation area during max elevation.

The position and velocity of the satellite were gained in the "Report and Graph manager" tool in STK. By choosing the satellite and the place alongside the corresponding time properties for maximum elevation, a "Position Velocity" report was generated, as seen in Figure 21. This report contains the position  $(x, y, z)$  in  $km$  and the velocity  $(vx, vy, vz)$  in  $km/s$ .

With this information, the quaternion were created with a script made by HYPSO.





**Figure 21:** "Position Velocity" report which shows time, position and velocity for HYPSON-1 at max elevation.

### 4.1.3 Quaternions

The script generating quaternions required several inputs, such as the capture scenario time, target location with latitude, longitude, and elevation, and the values from the "Position Velocity" report. After running the script, the quaternion were then generated as seen in Figure 22.

```

Quaternion:
0.99997932510585985 0.00628283051530189 0.00136945300943424 0.00000000000000000
--> HSI Off-Nadir Pointing Angle: 0.737

```

**Figure 22:** Generated quaternion to do a coordinate transformation from LVLH to the body frame.

### 4.1.4 Generating PC and FC scripts

Scripts had to be made for the PC and FC to share the mission planning information with the satellite. These scripts were made by HYPSON beforehand, thus, we had to fill in the correct parameters obtained from mission planning, such as the Unix time, pointing mode, file IDs, exposure, and quaternion components.

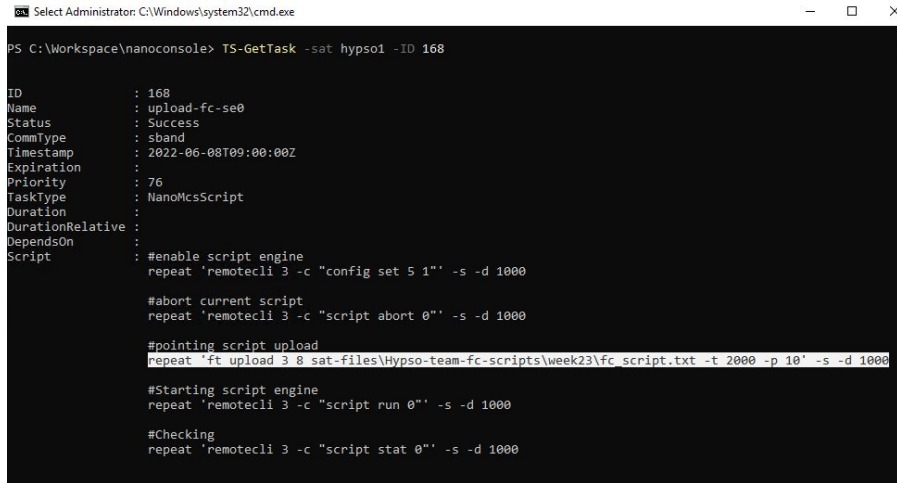
It was required to convert the max elevation time to Unix time to prepare for the scripts. Then we determined the type of satellite pointing technique we used, which in this case was quaternion pointing. The PC file IDs were set for storing captures, logs, telemetry, and timestamps. These FileID needed to be carefully selected, so they did not interfere with other planned captures. A delay timer could be set for downlinking if the capture was being taken at the same time the satellite was passing the ground station, as this could have created potential errors on the PC.

### 4.1.5 Scheduling and upload

We scheduled tasks to HYPSON-1 through "NanoMCS", a CLI used to perform uplinking of scripts and downlinking of housekeeping telemetry and data. We attend to present this process to validate Objectives 1 and 7 regarding scheduling and data transmission from a buffer.

---

The generated PC and FC scripts were uploaded to HYPSON-1 through nanoMCS by scheduling an uplink during the next pass over the ground station. The command "TS-GetTask -sat hypso1" returned the upcoming tasks to ensure we did not interfere with other planned operations. PC and FC scripts were uploaded to script engine 0 with corresponding File IDs. It was essential to check if these IDs were already in use for the next pass before scheduling new tasks, as new uploads would interfere. After determining the File IDs, we had to edit the upcoming tasks with the command "TS-EditScript -sat hypso1 -ID" to prepare the scheduling. The commands "TS-GetTask -sat -ID" displayed the upcoming tasks and ensured that the tasks were prepared for scheduling, as shown in Figure 23. Then we had to resume the tasks with the command "TS-ResumeTask -sat -ID" to order nanoMCS to upload the PC and FC scripts to script engine 0 during the next pass.



```
Select Administrator: C:\Windows\system32\cmd.exe
PS C:\Workspace\nanoconsole> TS-GetTask -sat hypso1 -ID 168

ID           : 168
Name        : upload-fc-se0
Status      : Success
CommType    : sband
Timestamp   : 2022-06-08T09:00:00Z
Expiration  :
Priority     : 76
TaskType    : NanoMcsScript
Duration    :
DurationRelative :
DependsOn   :
Script      : #enable script engine
              repeat 'remotecli 3 -c "config set 5 1" -s -d 1000

              #abort current script
              repeat 'remotecli 3 -c "script abort 0" -s -d 1000

              #pointing script upload
              repeat 'ft upload 3 8 sat-files\Hypso-team-fc-scripts\week23\fc_script.txt -t 2000 -p 10' -s -d 1000

              #Starting script engine
              repeat 'remotecli 3 -c "script run 0" -s -d 1000

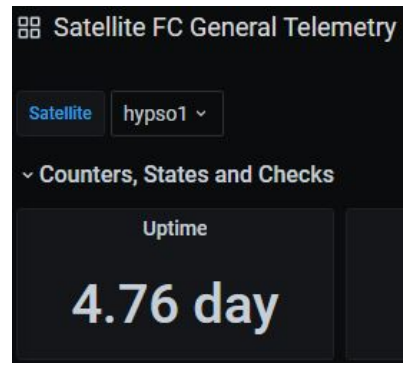
              #Checking
              repeat 'remotecli 3 -c "script stat 0" -s -d 1000
```

Figure 23: Command "TS-GetTask -sat hypso1 -ID 168". Displays task 168.

#### 4.1.6 Grafana - before and after a pass

Satellite configurations, telemetry, and activity needed to be checked several times daily to detect reboots and observe battery voltage and satellite pointing. The software "Grafana" tracked this. Here we specifically checked the up-time of PC and FC, ADCS telemetry from captures, and EPS status.

A reboot in the PC, FC or EPS could be a response to bugs in the uploaded capture scripts or indicate that something crucial needs to be troubleshooted, such as problems with the battery voltage or deterioration of instruments from e.g., radiation. In the case of a reboot, the scripts we made would need to be uploaded to the satellite once more. We checked for this by looking at the up-time of the PC and FC telemetry. Figure 24 shows that the PC and FC had not rebooted in the last 15 and 5 days, respectively.



**Figure 24:** Left: Current up-time PC. Right: Up-time FC. Both up-times were gathered on the 18th of June 2022.

Then we checked the ADCS telemetry and started by looking at the pointing target displayed in Figure 25. This graph tracked the type of satellite pointing that had been conducted. There were five pointing types, each corresponding to a specific y-axis value. These pointing modes are described in Table 2.



**Figure 25:** Pointing target values over time (18th of June 2022).

Value	Mode
15235	Ground station pointing
13541	Generic capture
12335	Sun charging mode
100	Slew capture
4	Quaternion pointing

**Table 2:** Pointing modes.

We also had to check the off-nadir angle to identify if the direction of the payload were correct during capture, tracked by the z-graph in Figure 26.

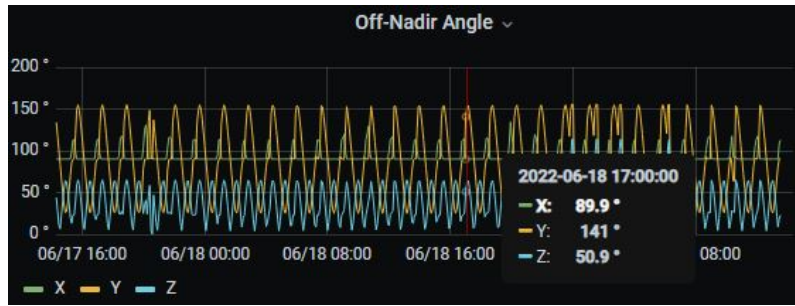


**Figure 26:** Off-nadir angles over time (18th of June 2022).

Next, we needed to check the battery voltage from EPS telemetry displayed in Figure 27. The maximum voltage of the HYPSON-1 satellite is 8.3 V, while everything above 7.6 V is considered operational, and the payload could be turned on during the next pass without problems. If the voltage drops below 7 V, we needed to wait until the solar panels had charged up the EPS above 7.6 V before turning on the OPU.

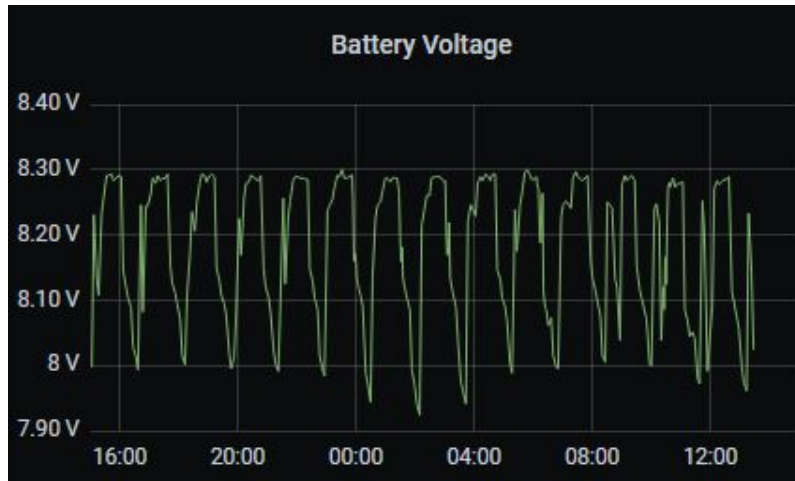


**Figure 27:** EPS battery voltage on the 16th to 17th of May.

The last thing we checked was the Power Channels Current which displayed the currents from the EPS. The OPU current is displayed in Figure 28 as "Out 10" and is the most vital current to monitor. This would tell us when the OPU had been turned on and for how long.

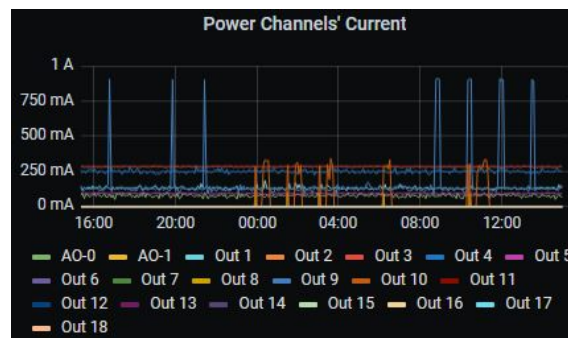


**Figure 28:** Currents from the EPS (16th to 17th of May 2022).

---

#### 4.1.7 During a pass

The way we observed the conducted tasks from current passes was through nanoMCS. Thus, knowledge about the status of uplinks, downlinks, and captures could be obtained. We could also backtrack through old sessions to display any failed tasks that might have occurred.

To get the session ID of the last passes, we entered the command "TS-GetSession -sat hypso1 -ID", which displayed all the tasks that were executed during the pass with the corresponding ID (Figure 29). It could be observed that the scheduling tasks for the PC and FC script with TaskID 168 and 169 were executed and successful. We then logged into the satellite during the next pass through "hypso-CLI" to check the status of script engine 0.

```
PS C:\Workspace\nanoconsole> TS-GetSession hypso1 3154
```

TaskID	TaskName	Status	Timestamp	Duration
29	eps-gs-wdt-reset	Success	2022-06-08T09:18:20Z	20.9s
30	comm-gs-wdt-reset	Success	2022-06-08T09:18:40Z	3.6s
31	srs4-gs-wdt-reset	Success	2022-06-08T09:18:43Z	2.9s
168	upload-fc-se0	Success	2022-06-08T09:18:45Z	11.7s
169	upload-pc-se0	Success	2022-06-08T09:18:56Z	13.4s
44	srs4-read-stats	Success	2022-06-08T09:19:09Z	5s
25	read-config-status	Success	2022-06-08T09:19:14Z	5.8s
24	read-configs	Success	2022-06-08T09:19:19Z	21s
27	read-versions	Success	2022-06-08T09:19:40Z	6.8s
26	check-time	Success	2022-06-08T09:19:46Z	12.1s
46	FT-FC-SE0-LOG	Success	2022-06-08T09:19:58Z	1.5s
200	FT-FC-SE1-LOG	Success	2022-06-08T09:19:59Z	1.8s
15	FT-EPS-Telemetry	Success	2022-06-08T09:20:00Z	3.2s
16	FT-COMM-1-Telemetry	Success	2022-06-08T09:20:03Z	1.9s
18	FT-FC-Telemetry	Success	2022-06-08T09:20:04Z	2.7s
51	FT-COMM-2-Telemetry	Success	2022-06-08T09:20:06Z	5s
20	FT-EPS-Startup-Telem	Success	2022-06-08T09:20:11Z	1.3s
21	FT-COMM-1-Startup-Telem	Success	2022-06-08T09:20:12Z	1.6s
23	FT-FC-Startup-Telem	Success	2022-06-08T09:20:13Z	2s
93	FT-PC-SE1-log-18	Success	2022-06-08T09:20:15Z	1.3s
76	FT-PC-SE0-log-17	Success	2022-06-08T09:20:16Z	2.1s
47	SE-status-FC-PC	Success	2022-06-08T09:20:18Z	5.8s
87	FT-PC-Telemetry	Success	2022-06-08T09:20:23Z	2.1s
88	FT-PC-Startup-Telem	Success	2022-06-08T09:20:25Z	1.4s
19	FT-FC-ADCS-Telemetry	Success	2022-06-08T09:20:26Z	5.8s
103	FT-PC-File-33	Success	2022-06-08T09:20:31Z	2.1s
104	FT-PC-File-34	Success	2022-06-08T09:20:33Z	1.4s
105	FT-PC-File-35	Success	2022-06-08T09:20:34Z	1.7s
106	FT-PC-File-36	Success	2022-06-08T09:20:35Z	2.1s
117	FT-PC-File-37	Success	2022-06-08T09:20:37Z	800ms
120	FT-PC-File-38	Success	2022-06-08T09:20:37Z	5m48s
123	FT-PC-File-39	Timeout	2022-06-08T09:26:25Z	3m44s

**Figure 29:** Command "TS-GetSession -sat hypso1 3154". Displays the tasks conducted during the session 3154.

Before we logged into the satellite we needed an Acquisition of Signal (AOS). This can be checked through "Satlab", which tracks the HYPISO-1 satellite. The satlab web page is displayed in Figure 30, and gave information that could validate Objectives 3-5 regarding S-band communication. When we had an AOS we checked the S-band spectrum to confirm the signal, displayed in Figure 31. From there we logged into the satellite through hypso-CLI to check the status of script engine 0. If it was "enabled" and "busy" for both PC and FC, we could be confident that the capture would happen during the specified timestamp. The following passes would then download the capture.

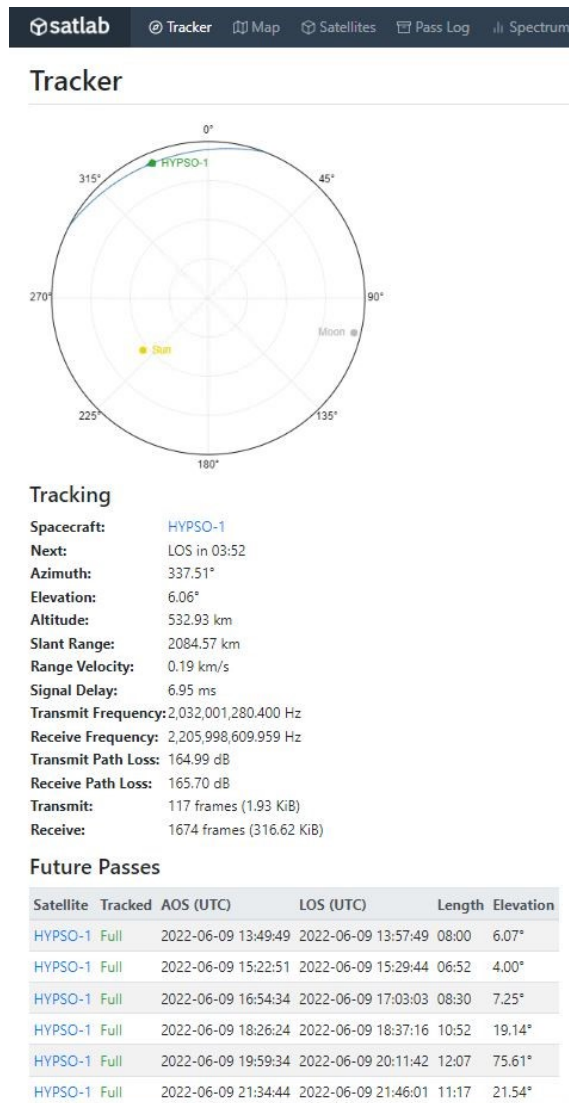


Figure 30: Satlab tracker for HYPSON-1.

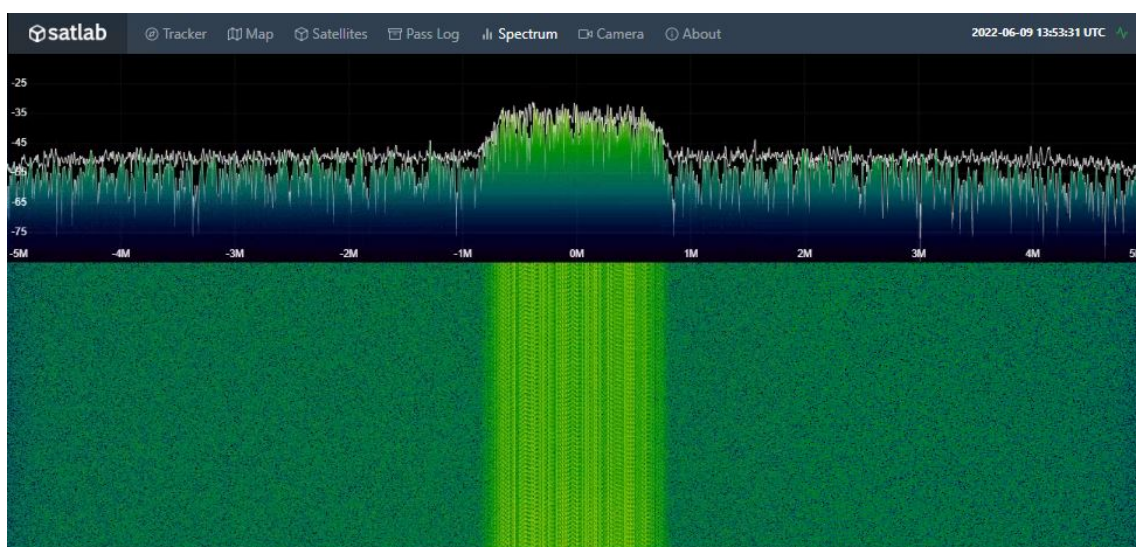


Figure 31: Signal from HYPSON-1 detected by Satlab.

---

Figure 29 displays several other tasks, such as downloading logs and telemetry. Furthermore, we were focused on TaskID 103, 104, 105, 106, 117, 120, 123, and 139, as these tasks downlinked the metazip and compressed captured data from HYPSONO-1 to the nanoMCS. Task 139 is not displayed as the above task timed out during the pass. By looking at the download duration of tasks 120 and 123, it could be determined that these files contained hyperspectral data. Task 120 finished during the pass, while task 123 timed out, which means it had to resume the download during the next pass, assuming all other tasks with higher priority had finished their download.

#### 4.1.8 Pull from nanoMCS

The data downlinked from HYPSONO-1 were stored in a nanoMCS database. Pulling the data let us acquire the logs, telemetry, and captured data to analyze it. This gave us all the information needed to determine whether the capture was successful and helped us validate Objectives 7, 10, and 11 regarding logged timestamps, size, and housekeeping telemetry, respectively.

We did this by defining which buffer File ID we wished to pull data from and when it was acquired. For instance, the capture over Frohavet on the 17th of May 2022 was downlinked to buffer File ID 34 (metazip) and 38 (compressed), and the download finished at 17:21:25. The File ID's were determined in mission planning.

Finally, we had to extract the data from the metazip, decompress the compressed cube, and create an RGB representation of the captured area. These tasks were done by using scripts created by HYPSONO. We then double-checked the timestamps of the capture by checking the extracted file "timestamp\_services" and converted the capture start Unix time to human-readable time.

#### 4.1.9 Delete safe copies and download logs

After receiving the data, we had to delete safe copies on the OPU during the following pass. Then we downloaded logs from the OPU necessary for troubleshooting operations' potential errors. The purpose of this operation was to clear up space on the satellite and remove cluttering, to prepare for future captures.

After obtaining an AOS, we turned on the payload through "hypso-CLI". The command told the EPS to turn on the OPU from the EPS output channel. Then we had to confirm the connection with the OPU by pinging the system's corresponding CSP address until we got an acknowledgment. When we received an acknowledge in return, as shown in Figure 32, we set the OPU power off timer to ensure proper system shutdown after the pass. Figure 33 shows the highlighted output channel 10, indicating that the OPU got current "I (mA)" and that the power-off timer "Toff (s)" was set. The power-off timer was necessary because the OPU demanded a large amount of power. The OPU would power off after 40 minutes if it was not set.

```
(hypso-cli-SBAND) csp ping 12
Pinging node OPU (12)...
Ping received from OPU (12) after 174 ms.
```

**Figure 32:** Command "csp ping 12" which returns an acknowledge if the OPU is turned on and we have an connection. As we received a ping after 174 *ms* we know we had contact.

```
(hypso-cli-SBAND) shell remote oneshot 4 5 hkout
```

OUTPUTS

Output	State	L_up	Faults	Ton (s)	Toff (s)	I (mA)	Converter
AO_3.3V	-	-	-	-	-	98	3341
AO_5V	-	-	-	-	-	0	4982
1	1	0	0	0	0	119	4982
2	0	0	0	0	0	0	4982
3	1	0	0	0	0	281	5009
4	1	0	0	0	0	247	3341
5	1	0	0	0	0	96	3341
6	0	0	0	0	0	0	5009
7	0	0	0	0	2462	0	5009
8	0	0	0	0	2462	0	12089
9	1	0	0	0	0	900	12089
10	1	0	0	0	729	279	bat

OUTPUT CONVERTERS

Converter	1	2	3	4
U (mV)	3341	4982	5009	12089
State	ON	ON	ON	ON

OK

**Figure 33:** Command "shell remote oneshot 4 3 hkout" which returns the EPS output channels. The highlighted line is the output channel to the OPU.

Now that the prerequisites were set, we could remove the safe copies. Figure 34 displays the files currently on the OPU. We then searched for the safe copies with the timestamp corresponding to our captures and removed the files. The next step was to extract the logs folder. After confirming that the logs had been correctly downlinked, we entered the commands to delete them from the OPU.

```
(hypso-cli-SBAND) shell remote oneshot 12 6 ls -l
```

```
drwxrwxrwx  2 root  root           4096 May 27 08:59 capture-20220527T085908Z
drwxr-xr-x  2 root  root           4096 May 27 10:25 capture-20220527T102526Z
drwxr-xr-x  2 root  root           4096 May 27 11:58 capture-20220527T115837Z
drwxr-xr-x  2 root  root           4096 May 27 13:36 capture-20220527T133613Z
-rw-r--r--  1 root  root      54541312 Jun  7 19:00 capture-20220527T133613Z.tar
drwxr-xr-x  2 root  root           4096 May 27 18:15 capture-20220527T181520Z
drwxr-xr-x  2 root  root           4096 May 28 11:47 capture-20220528T114718Z
-rw-r--r--  1 root  root      63023616 Jun  7 20:35 capture-20220528T114718Z.tar
drwxrwxrwx  2 root  root           4096 May 28 13:21 capture-20220528T132138Z
drwxrwxrwx  2 root  root           4096 May 28 18:03 capture-20220528T180400Z
drwxr-xr-x  2 root  root           4096 May 28 19:38 capture-20220528T193828Z
drwxr-xr-x  2 root  root           4096 May 29 11:35 capture-20220529T113555Z
```

**Figure 34:** Command "shell remote oneshot 12 3 ls -l" to display the safe copies on the OPU.

#### 4.1.10 Georeferencing

To validate Object 24 under "Georeferencing," we had first to extract the RGB composed image alongside its center coordinates inputted in Google Maps (Figure 35). Then, a text file "footprint.txt," containing the latitude and longitude for all the captured pixels, was used to transform pixel indices to geodetic latitude and longitude, creating the georeferenced image. This image was created by Dennis D. Langer from HYPSON and is depicted in Figure 36. Section 6 will discuss why the two Figures do not match.





**Figure 35:** Left: RGB composite of the Frohavet capture. Right: Google Maps image of the captured center location for the Frohavet capture.

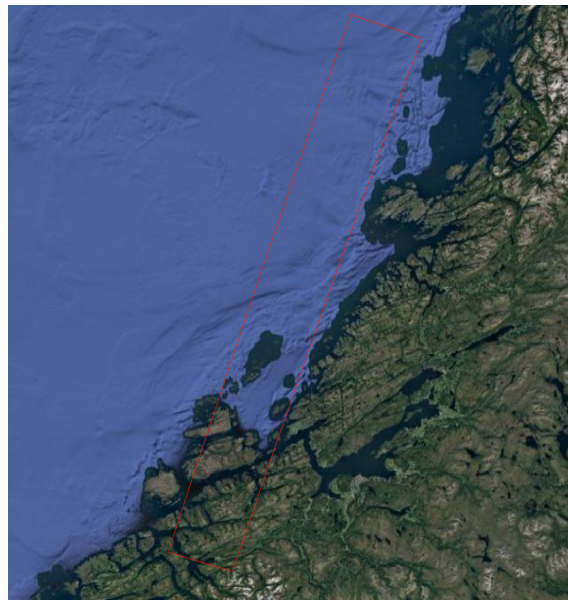


**Figure 36:** Georeferenced image of the Frohavet capture.

Now that all the data is obtained and removed from the satellite, the next step is to analyze the captured hyperspectral image. However, the data must first be corrected with radiometric and spectral calibration.

---

## 4.2 Analysis

The following section uses the software SNAP and Excel to analyse and visualize the HSI data. These sections are presented to evaluate the Objectives 14-23 regarding calibration, analysis and radiance to reflectance.

### 4.2.1 Startup

The calibrated data was uploaded to SNAP as a .bip file with a corresponding header. The header file characterized the information given in the .bip file and had to be constructed with the parameters: bands, lines, samples, byte order, interleave, header offset, data type, wavelength units, and wavelength. We could open the file in SNAP by assigning the parameters as depicted in Figure 37.

Name	Value
bands	120
lines	956
samples	684
byte order	0
interleave	bip
header offset	0
data type	12
wavelength units	nm
wavelength	388.0417142, 391.5863558, 395.1299309, 398.6724394, 402.2

**Figure 37:** Header file Frohavet SNAP.

By combining the bands for Red (630 nm), Green (550 nm), and Blue (480 nm), we got the RGB composite of the HSI data over Frohavet. This is depicted in Figure 38.

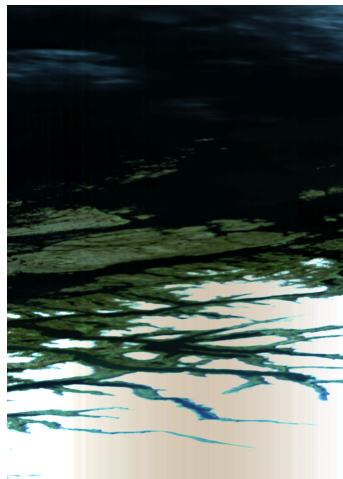


**Figure 38:** RGB composite of Frohavet. The snow pixels are over saturated after calibration.

We could then apply a mask over clouds, cirrus clouds, snow, shores, and land to the image as we primarily wanted to analyze the ocean.

---

### 4.2.2 Masking

Objects we do not want to analyze could interfere with the ocean, creating significant inaccuracies in the analyzed data. Thus, we wanted to mask these objects beforehand.

The Spectrum View tool allowed us to see the pixel spectral intensity for each wavelength. We could then determine what bands represented the different types of objects. We also wanted to be strict with which pixels were masked and not so that, for instance, cirrus clouds were masked, as well as rocks and small islands. Figure 39 shows the objects clouds, ocean, snow, and land being selected by pins, and their spectral intensity is represented in Figure 40. After analyzing the Spectrum View, it was determined that band 76, representing the wavelength  $651\text{ nm}$  was a fit option to distinguish the ocean from the other objects. By setting the minimum value of the spectral radiance to be  $13.5\text{ (mW)/(m}^2 \times \text{sr} \times \text{nm)}$ , we got the mask depicted in the middle image of Figure 41. Then by reversing the mask, as shown in the right image in Figure 41, we now had a region of interest (ROI) that we wanted to analyze further. This region mostly contained ocean pixels, with a small amount including cirrus clouds and shores. The rest of the pixels in the image were removed.

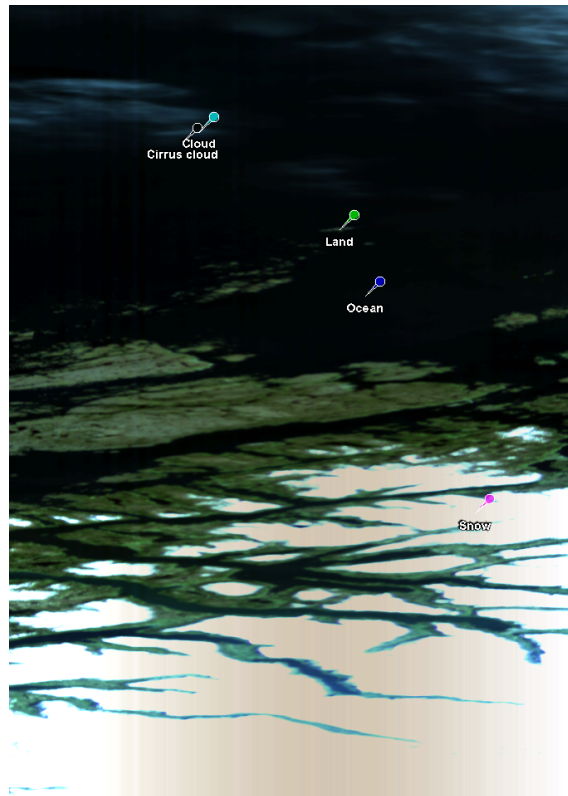


**Figure 39:** RGB composite of Frohavet with cloud, cirrus cloud, ocean, snow and land pixels pinned.

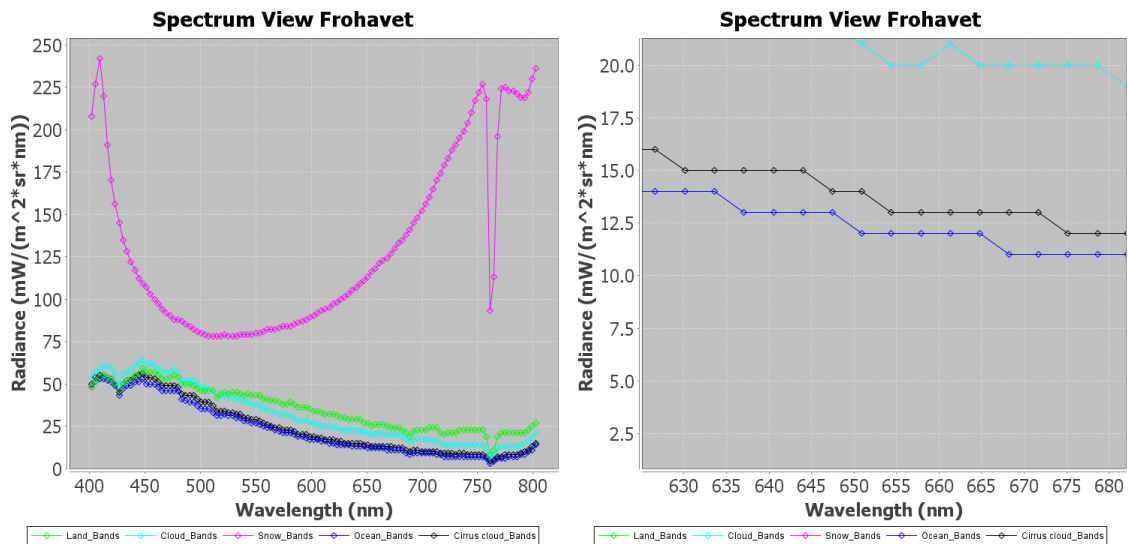


**Figure 40:** Left: Spectral view of Frohavet with cirrus clouds (light blue), ocean (blue), snow (purple) and land (green) pixels pinned. The spectrum of snow is unrealistic due to the over saturation. Right: Zoomed in on 651 nm to distinguish thin cirrus clouds and ocean pixels.

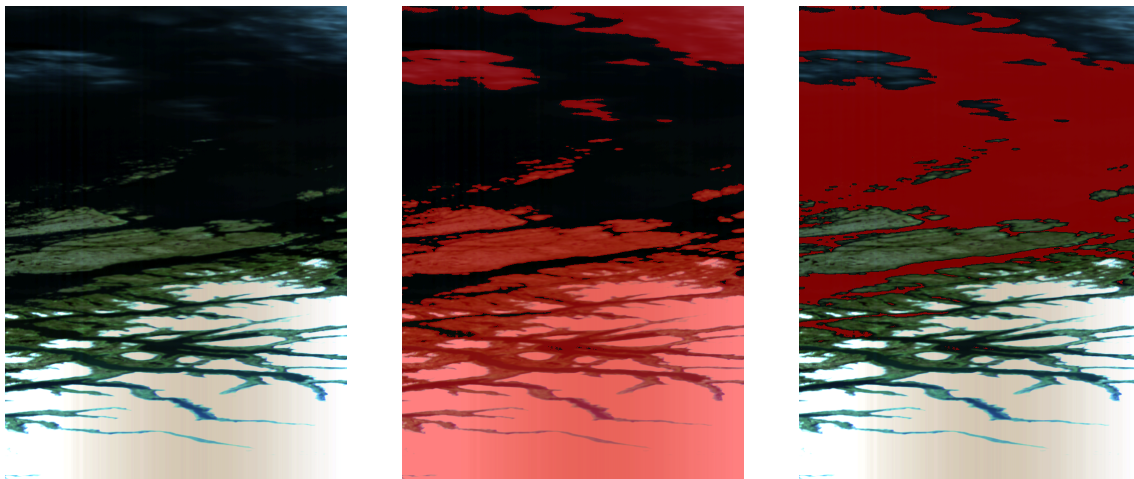


**Figure 41:** Left: Hyperspectral image of Frohavet. Middle: Hyperspectral image of Frohavet applied with cloud, cirrus cloud, snow, shore and land mask. Right: Hyperspectral image of Frohavet with a reversed mask, representing the ocean.

### 4.2.3 Unsupervised classification and PCA

The unsupervised classification algorithm k-means, presented in chapter 2.6, were applied four times to the Frohavet capture in SNAP. The first two were run on the whole image without a mask, with 8 and 10 output clusters, respectively. The third analysis was run on the masked capture, and the last was run on the masked capture with PCA applied beforehand, both with eight output clusters. All the classifications used 30 iterations. All the 120 source bands were used as input for the first three classifications, while the last one used the first three PCA components.

The PCA on the Frohavet capture was also done in SNAP. The input was all the 120 source bands with a set output component count of 5. The PCA was run with and without the cover mask.

---

SNAP created an analysis for each cluster after the classification, which told us the spectral value of the cluster center. This was the mean spectral value of every band relative to their cluster. For PCA, we got the eigenvectors that showed the directions in which our new data were dispersed. We will show and analyze these values later on.

#### 4.2.4 Radiance to reflectance

Following the radiance to reflectance conversion introduced in chapter 2.8, we needed the HSI radiance, solar spectral irradiance  $E_0$ , and the solar zenith angle  $\theta$ . The solar spectral irradiance values were obtained by using the NASA-PACE satellite. The orbit is sun-synchronous with an inclination of  $98^\circ$ , similar to HYPSON-1 [48]. The altitude of NASA-PACE is  $676.5 \text{ km}$ , while HYPSON-1 has an altitude of  $525 \text{ km}$ . The spatial interval of the wavelengths is  $2.5 \text{ nm}$  for NASA-PACE and about  $3.5 \text{ nm}$  for the HSI.

The solar spectral irradiance values from NASA-PACE collected from *Ocean Color Web* [49], were interpolated with the wavelengths of the two satellites in *Excel*, using a linear interpolation function *FORECAST.LINEAR*. Based on existing values the function predicted a value along a linear trend [50].

The sun zenith angle  $\theta$  was obtained using a solar position calculator from *University of Oregon Solar Radiation Monitoring Laboratory* [51]. By inputting the location and time of capture, we got the solar zenith angle in degrees, which we converted to radians.

The reflectance for each band was then calculated by the following equation 13 and plotted in *Excel*.

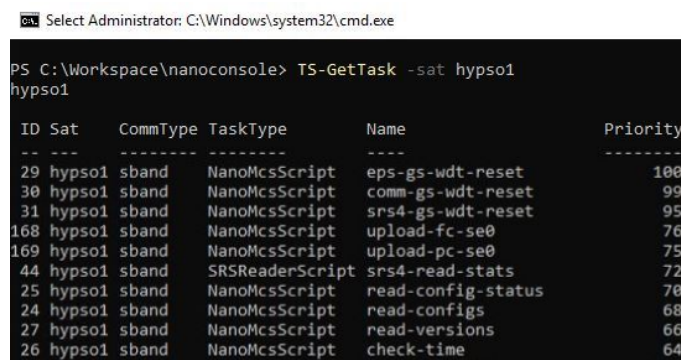
---

## 5 Results

The following section, combined with section 6, will evaluate which objectives HYPPO-1 meets and how its performance can be improved based on the experiments in section 7 and the corresponding results.

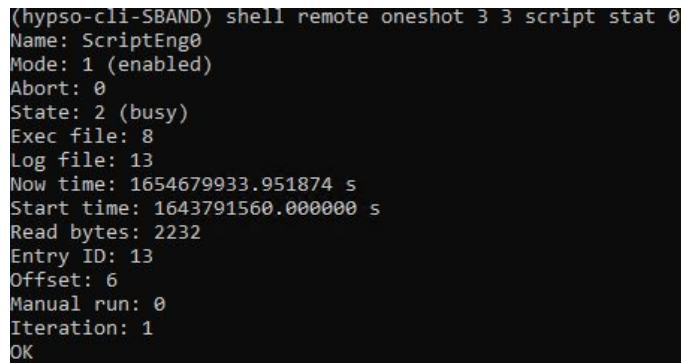
### 5.1 Results from operations

To conclude whether mission planning and operations had succeeded, we had to check for new scheduled uploading tasks, the state of script engine 0, and the Unix time from the downloaded metazip. First, we use the command "TS-GetTask -sat hypso1" to check if the uploading tasks 168 and 169 are scheduled for the next pass. This command returns Figure 42. Then, while we were in a pass and had AOS, we turned on the OPU to check the state of script engine 0 (Figure 43). Lastly, after pulling the downloaded data from NanoMCS, we checked the Unix timestamp of the capture duration by converting it to human-readable time. The Unix time for capture start and end were 1652783039 and 1652783087, which corresponded to the time interval 10:23:59-10:24:47 on the 17th of May 2022.



```
Select Administrator: C:\Windows\system32\cmd.exe
PS C:\Workspace\nanoconsole> TS-GetTask -sat hypso1
hypso1
ID Sat    CommType TaskType      Name                                Priority
-----
29 hypso1  sband      NanoMcsScript eps-gs-wdt-reset                    100
30 hypso1  sband      NanoMcsScript comm-gs-wdt-reset                    99
31 hypso1  sband      NanoMcsScript srs4-gs-wdt-reset                    95
168 hypso1  sband      NanoMcsScript upload-fc-se0                        76
169 hypso1  sband      NanoMcsScript upload-pc-se0                        75
44 hypso1  sband      SRSReaderScript srs4-read-stats                      72
25 hypso1  sband      NanoMcsScript read-config-status                  70
24 hypso1  sband      NanoMcsScript read-configs                         68
27 hypso1  sband      NanoMcsScript read-versions                         66
26 hypso1  sband      NanoMcsScript check-time                       64
```

**Figure 42:** Command "TS-GetTask -sat hypso1" after scheduling the upload of the PC and FC scripts.



```
(hypso-cli-SBAND) shell remote oneshot 3 3 script stat 0
Name: ScriptEng0
Mode: 1 (enabled)
Abort: 0
State: 2 (busy)
Exec file: 8
Log file: 13
Now time: 1654679933.951874 s
Start time: 1643791560.000000 s
Read bytes: 2232
Entry ID: 13
Offset: 6
Manual run: 0
Iteration: 1
OK
```

**Figure 43:** Command "shell remote oneshot 3 3 script stat 0" to check the status of script engine 0 for the FC script.

---

### 5.1.1 Download time

The Frohavet capture cube was downloaded from TaskID 123, which can be confirmed with the command "TS-GetSession hypso1 ID". It returned the tasks that had been conducted during a satellite pass. Figure 44 depicts task 123 from the sessions 2660, 2662 and 2664. During the first session, 2660, the status is stated as "Failure" due to the captured image being taken during this period. Session 2662 returned the status "Timeout" as the download did not finish during this pass. The last session 2664 completed the download as the status is stated as "Success". Thus, the overall download period during AOS was 11 minutes, while the download period since the end of capture was 3 hours, 4 minutes, and 17 seconds. The size of the compressed cube was 66.5 MB.

```
PS C:\Workspace\nanoconsole> TS-GetSession hypso1 2660
TaskID TaskName          Status  Timestamp          Duration
-----
123 FT-PC-File-39      Failure 2022-05-17T10:24:04Z 1.6s
PS C:\Workspace\nanoconsole> TS-GetSession hypso1 2662
TaskID TaskName          Status  Timestamp          Duration
-----
123 FT-PC-File-39      Timeout 2022-05-17T11:56:36Z 7m6s
PS C:\Workspace\nanoconsole> TS-GetSession hypso1 2664
TaskID TaskName          Status  Timestamp          Duration
-----
123 FT-PC-File-39      Success 2022-05-17T13:29:04Z 3m53.8s
```

**Figure 44:** Merged image of the download sessions 2660, 2662 and 2664 corresponding to the three consecutive passes that downloaded the Frohavet capture.

### 5.1.2 Grafana

It was also necessary to check Grafana for pointing errors, off-nadir angles, and EPS output currents. Figure 45 states that during the Frohavet capture, the pointing target value was 4, which is referred to as a quaternion pointing in table 2.

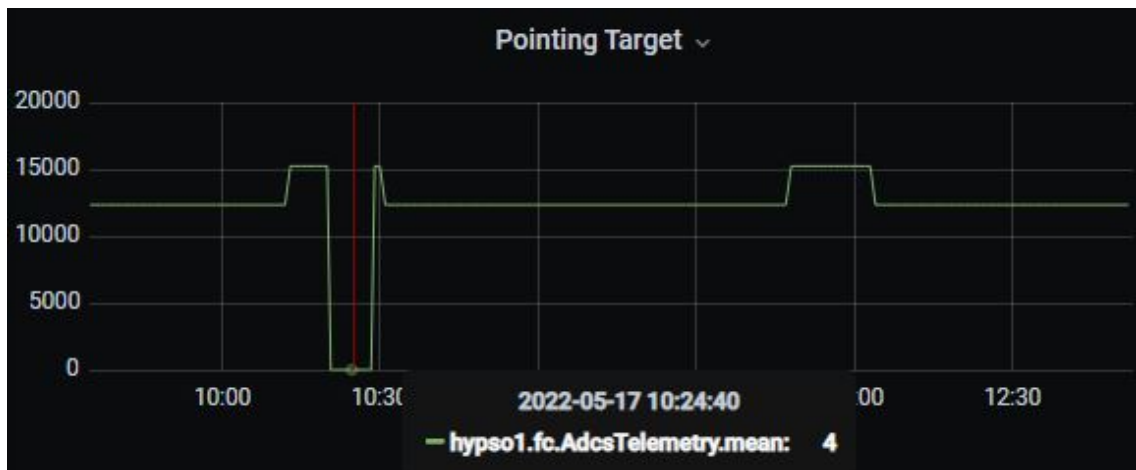
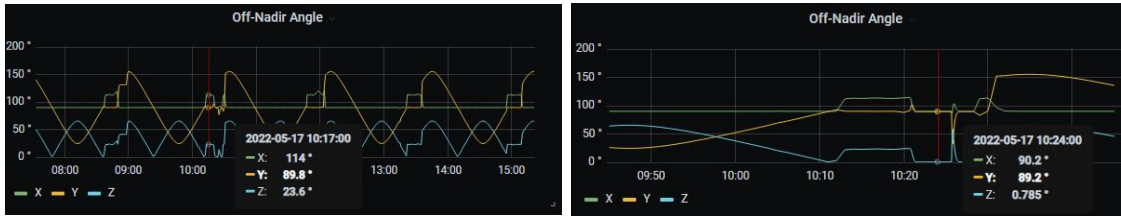


**Figure 45:** Pointing target value on the 17th of May 2022.

Figure 46 states that the z-value during capture, referred to as the direction of the payload, were 0.785°.

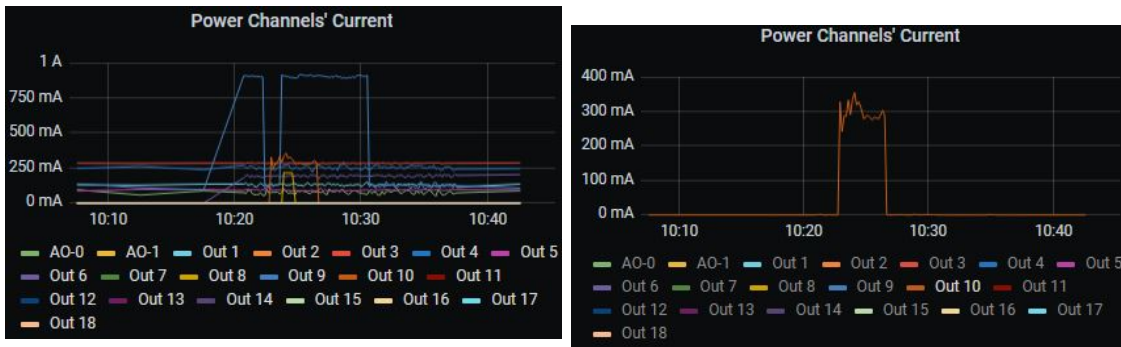


(a) Off-nadir angles on the 17th of May 2022.

(b) Zoomed to the time of capture.

**Figure 46:** Off-nadir angles during 17th of May 2022

Also, Figure 47 states the value of the EPS output current to the different power channels during capture.



(a) EPS power channel currents displayed from about 10:10-10:40 on the 17th of May 2022.

(b) Focused on the OPU's current.

**Figure 47:** Instrument currents from the EPS during Frohavet capture 17th of May 2022.

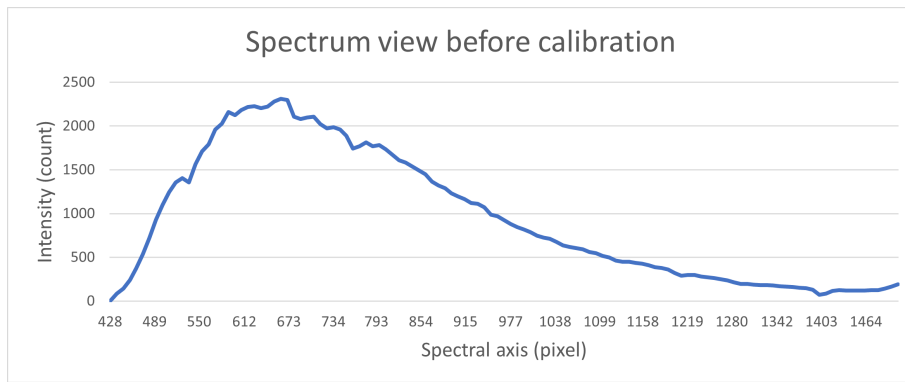
## 5.2 Results from calibration and analysis of Frohavet

This section first states the results from the radiometric and spectral calibration of the Frohavet capture. Then it states the results from the analysis and follows the step-by-step process from chapter 4.2.

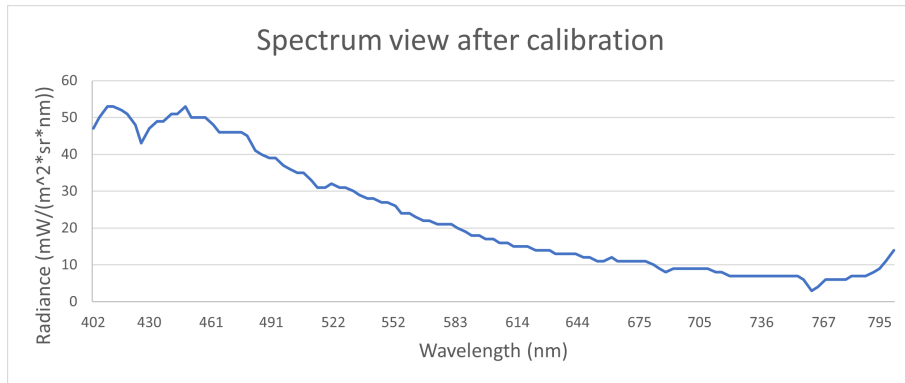
### 5.2.1 Radiometric and spectral calibration results

An ocean pixel was chosen to be analyzed before and after radiometric and spectral calibration. Figure 48a depicts the intensity value of each pixel, while Figure 48b depicts the radiance values for each wavelength after the calibration was conducted.





(a) Spectrum view of Frohavet before calibration.

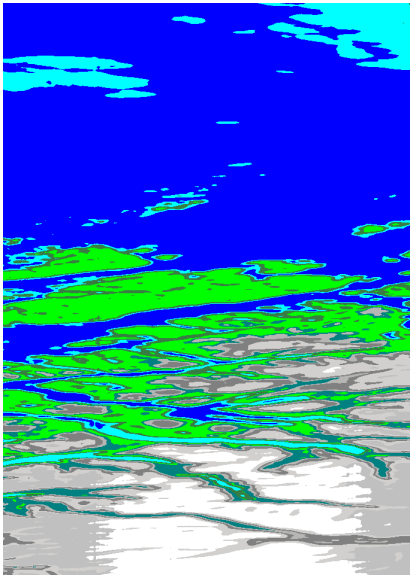


(b) Spectrum view of Frohavet after calibration.

**Figure 48:** The spectrum of a pixel from Frohavet before and after radiometric and spectral calibration.

### 5.2.2 Unsupervised classification results

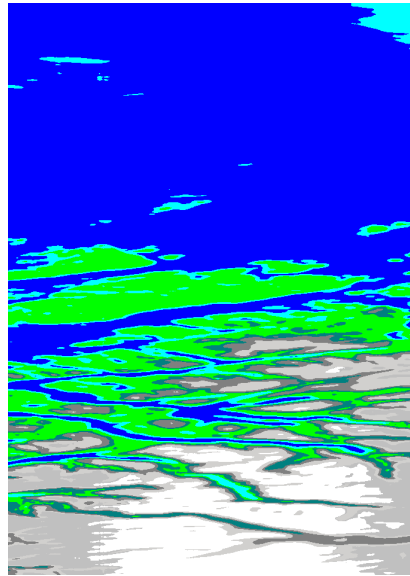
By inputting the calibrated Frohavet scene with ten output clusters, the resulting classified image is depicted in Figure 49a, with its corresponding class indices in Figure 49c. Figure 49b shows the classified image with 8 clusters with the corresponding class indices in Figure 49d.



(a) Classification with 10 clusters as output.

Label	Colour	Value	Frequency
Ocean	0	44.858%	
Land	1	11.153%	
Snow/Clouds 1	2	8.182%	
Cirrus clouds and shores 1	3	8.004%	
Snow/Clouds 2	4	6.335%	
Snow/Clouds 3	5	4.889%	
Shores 2	6	5.087%	
Snow/Clouds 4	7	4.304%	
Land close to snow/clouds	8	4.209%	
Snow/Clouds 5	9	2.980%	

(c) Class indices of Figure (a).



(b) Classification with 8 clusters as output.

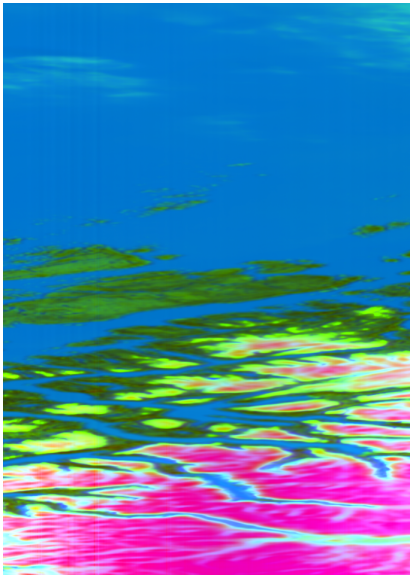
Label	Colour	Value	Frequency
Ocean	0	50.261%	
Land	1	13.800%	
Snow/Clouds 1	2	8.743%	
Cirrus clouds and shores	3	6.577%	
Snow/Clouds 2	4	6.425%	
Snow/Clouds 3	5	5.160%	
Snow/Clouds 4	6	4.656%	
Land close to snow/clouds	7	4.377%	

(d) Class indices of Figure (b).

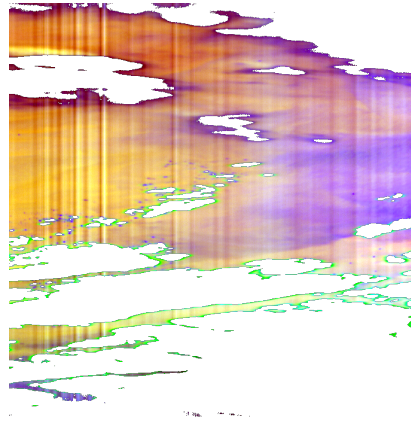
**Figure 49:** Unsupervised classification of Frohavet.

### 5.2.3 PCA results

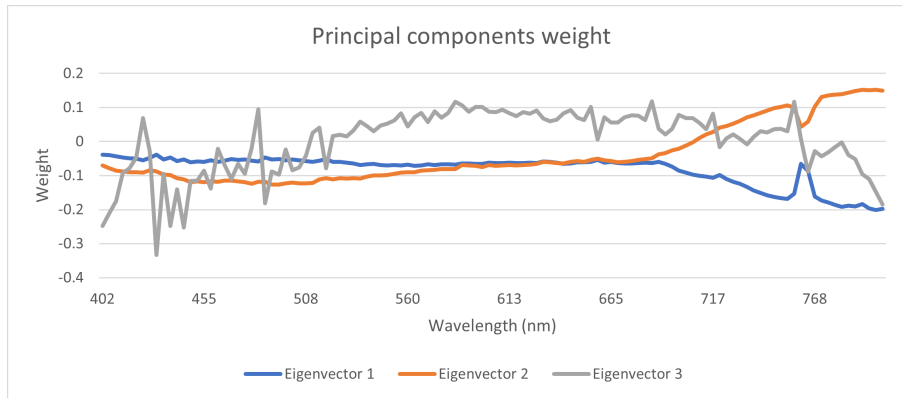
The resulting images from the PCA on the Frohavet scene are depicted with an RGB composite in Figure 50a. Figure 50b depicts the PCA RGB composite of the Frohavet scene with a mask applied over land, clouds and snow. Both the images are composed of the first three PCA components so that the RGB is respectively component 1, component 2, and component 3. Figure 50c depicts the weights of the principal components (eigenvectors) for Figure 50b, showing the directions our data were dispersed.



(a) PCA without cover mask.



(b) PCA with cover mask.

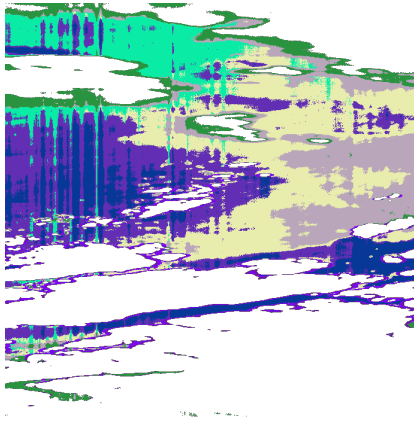


(c) Weights of the principal components in Figure (b).

**Figure 50:** Principal component analysis.

#### 5.2.4 Unsupervised classification results of the masked and compressed Frohavet scene

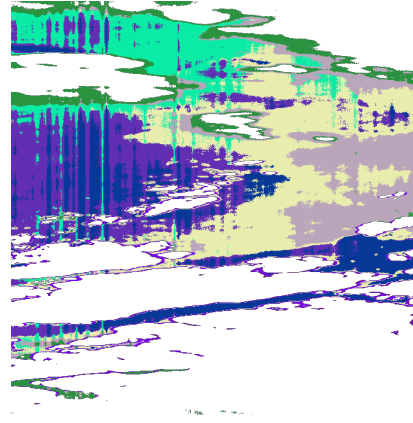
The result of unsupervised classification on the masked Frohavet scene is depicted in Figure 51a with its class indices in Figure 51c. The computation time was 63 seconds with all the 120 bands as input. Applying the PCA compression first reduced the computation time to 6 seconds, and its classified image is depicted with its class indices in Figure 51b and 51d. Both classifications had eight output clusters.



(a) Classification of a masked Frohavet scene.

Label	Colour	Value	Frequency
class_1		0	23.947%
class_2		1	22.098%
class_3		2	15.334%
class_4		3	11.600%
class_5		4	13.284%
class_6		5	8.650%
class_7		6	3.348%
class_8		7	1.738%

(c) Class indices of Figure (a).



(b) Classification of a masked Frohavet scene with PCA beforehand.

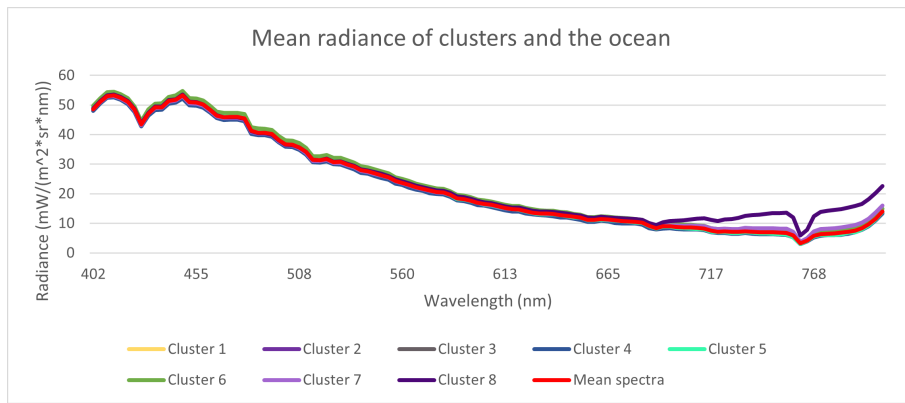
Label	Colour	Value	Frequency
class_1		0	24.394%
class_2		1	20.476%
class_3		2	15.689%
class_4		3	12.567%
class_5		4	14.630%
class_6		5	8.497%
class_7		6	2.681%
class_8		7	1.065%

(d) Class indices of Figure (b).

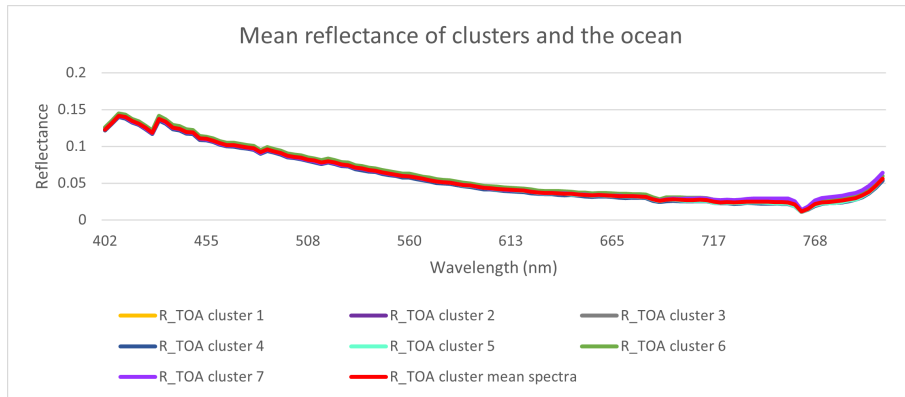
**Figure 51:** Unsupervised classification of Frohavet.

### 5.2.5 Radiance and reflectance of the masked Frohavet scene

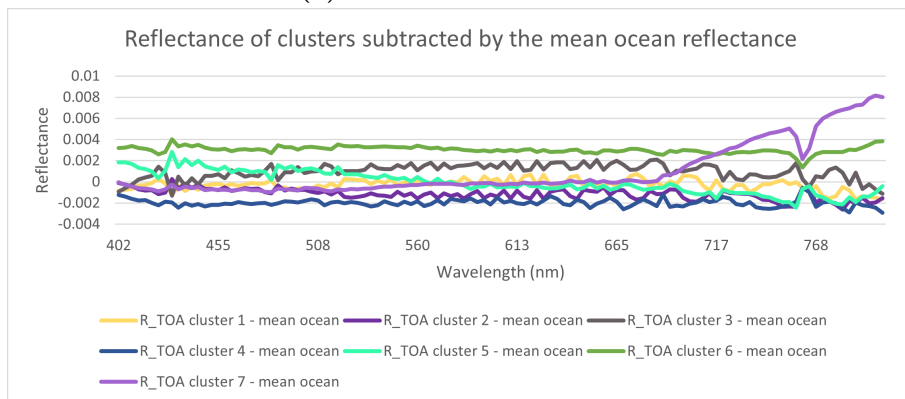
The clusters spectral radiance and reflectance values for each wavelengths are depicted in Figures 52a and 52b. These graphs also show the mean spectral radiance and reflectance value for the Frohavet ocean as a comparison. In Figure 52c cluster 8 is removed while the mean ocean reflectance subtracts the rest to manifest the clusters' spectral signatures. To get the reflectance values, we used equation 13 with a solar zenith angle of  $45.4^\circ$ , which corresponded to the location and time of capture. The solar irradiance values were taken from NASA-PACE [49].



(a) Cluster mean radiance.



(b) Cluster mean reflectance.



(c) Cluster mean reflectance subtracted by the mean ocean reflectance.

**Figure 52:** Radiance and reflectance of Frohavet.

---

## 6 Discussion

This section discusses the results from the previous section to evaluate which objectives HYPSON-1 meets and how its performance can be improved based on the experiments conducted in sections 4.1 and 4.2. The first subsection presents a general discussion about operations and georeferencing, then it evaluates the corresponding objectives. The following two subsections are structured the same way, presenting calibration and analysis, respectively. The last section discusses the applicability for the software used in this thesis.

### 6.1 Operations

The Frohavet scene was chosen to be the primary scene for analysis in this thesis as NTNU's Mission Control Center has deployed supporting robotic assets for in-situ observations in the area. The location close to Frøya is interesting to observe as supporting sampling and underwater imaging from AUV field campaigns are run regularly by NTNU. Furthermore, alongside in-situ measurements, the date of capture (17th of May 2022) had clear weather and near nadir imaging. After capture, we had to ensure that the image was correctly georeferenced.

#### 6.1.1 Mission planning, scheduling and downlinking data

Georeferencing could give an answer to whether or not mission planning was successful and up-linked correctly. However, the georeferencing for the Frohavet capture was incorrect due to improper time synchronization at the time of capture. This error is displayed in Figure 36 where it suggests that the capture starting point was far more North-East than what Figure 35 confirms. Therefore, we compared the Unix time and the off-nadir angle from mission planning, to the downloaded telemetry. The logged timestamps downloaded from nanoMCS of the Frohavet capture stated that the capture was from 10:23:59 to 10:24:47. From mission planning we know that center imaging and max elevation was at 10:24:21.5. We noticed that the timestamp of the center image was 21.5 seconds from the start of capture, and 25.5 seconds from the end of capture, which was not correct. This was due to STK constantly updating its tracking of the HYPSON-1 orbit. Figure 19 was generated on the 6th of June 2022 for this thesis, however, the actual Access report made for this capture was generated on the 13th of May 2022. By looking up the correct Access report on HYPSON's GitHub, we found that the correct timestamp for center imaging was 10:24:23, 24 seconds from both the start and end of capture.

We speculate that the Access report differed because STK calculated the max elevation in advance and was not completely precise compared to the live updates from Grafana. The closer to the capture date, the more accurate STK became because the Two Line Elements (TLEs), which describe the orbital elements of HYPSON-1, must be updated regularly. The TLEs use a prediction formula to estimate, to some accuracy, the position and velocity of HYPSON-1 at any given point in the past or future [52]. From this standpoint, early mission planning can be considered a potential error. Thus, mission planning must be performed as close to possible capture time to get the most accurate captures. This error was also replicated for the off-nadir angle.

The ground center imaging point's max elevation from the Access report was  $89.252^\circ$ , which was equal to  $0.748^\circ$  off-nadir from the satellite's perspective. The off-nadir direction

---

of the payload during capture tracked by Grafana was  $0.785^\circ$ . The correct Access report used for the mission stated that the max elevation was  $89.211^\circ$ , or  $0.789^\circ$  off-nadir relative to the satellite. The error in the off-nadir angle appears to be minor fluctuations in the payload direction during pointing. This was most likely due to vibrations as the satellite maneuvered to get into the exact position throughout the capture, and is therefore not to be of concern. Also, this fluctuation with a  $0.004^\circ$  shift from  $500\text{ km}$  away can, with basic trigonometry, be translated to only 35 meters. Note that this excludes the curvature of the Earth, which is insignificant at this distance. Thus we can conclude that there were no unexpected control errors before or during pointing.

### 6.1.2 Monitoring correct scheduling

To determine successful scheduling we had to look at the scheduled tasks in Figure 42 and the state of the script engines in Figure 43. It can be confirmed that the commands used for scheduling the uploads of the PC and FC scripts were successful by observing that tasks 168 and 169 were scheduled for the next pass. By logging into the satellite through hypso-cli, we observed that the task was indeed uploaded, and that "Mode: 1" was "enabled" and "State: 2" was "busy" for both the FC and PC.

### 6.1.3 Troubleshooting HYP SO-1 capture errors

Even though the script engines stated that the tasks were scheduled, errors in the capture could still occur. Through chapter 4.1 we displayed several methods used for troubleshooting. These methods included checking quaternions, off-nadir angle, georeferencing, Unix times, and the current from the EPS to the OPU. Operators can also use nanoMCS to see previous sessions and scheduled tasks, and hypso-CLI to follow the upcoming passes. Monitoring the HYP SO-1 systems is accessible with these command line interfaces, ensuring thorough error research if necessary.

### 6.1.4 Requirements of operations

A part of Objective 1 from chapter 1.3.1 states that HYP SO-1 shall enable flexible mission planning & scheduling through successfully integrated up-linked mission data. From the section above, we can confirm that the capture timestamps were correct, that the off-nadir angle during capture was sufficient, and that scheduling worked as intended. We believe that correct timestamp and off-nadir pointing justifies a successful up-link of mission planning and scheduling. However, georeferencing must be correct to determine whether or not this part of Objective 1 is approved.

Objective 2 requires in-orbit software updates on the OPU, which were not conducted during the operation period since launch. However, we have tested that file uploads to the satellite work. Furthermore, all the functionality was tested on-ground, meaning these functionalities are ready for deployment on the satellite as soon as possible. Thus, Objective 2 is currently not satisfied.

Objective 3, 4, and 5, are regarding communication through the S-band. Objective 3 is satisfied as all communication we have conducted with the satellite was through the S-band. Objective 4 demands an S-band down-link within the band  $2,200\text{--}2,290\text{ MHz}$  with a bit rate of at least  $800\text{ Kbps}$ , while Objective 5 demands the S-band up-link to be within the

---

band 2,025-2,110 *MHz*. These requirements can be checked through Satlab in Figure 30. It states that the transmit frequency (up-link) was 2,032 *MHz*, while the receive frequency (down-link) was 2,206 *MHz*. By opening the Satlab HYPSON-1 settings, we could observe the downlink bit rate to be 1400000 baud data-rate, as depicted in Figure 53. This is equal to 1.4 *Mbps*, thus, all the requirements for Objectives 3-5 are met.

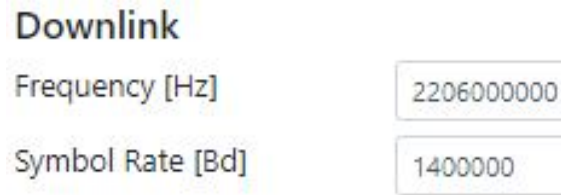


**Figure 53:** S-band downlink frequency and bit rate.

Objective 6 requires us to log the received data to a file for archiving with timestamps. This is because it is helpful for the spacecraft and users to have historical data. These timestamps were downloaded through a metazip that was unzipped with the command "tar -xf metazip\_frohavet\_2022-05-17.tar". We then got the folder "hsi0," containing the file "timestamps\_services." This file contained the Unix timestamps for when each frame was taken by the HSI, as well as capture start and end. It was confirmed above that the capture start and end timestamps were correct. By checking the number of frames taken and dividing it by 2, we got the logged timestamp for the capture center. This was logged as frame number 478 with the Unix timestamp 1652783063, which converts to the time 10:24:23 on the 17th of May 2022. We can therefore conclude that Objective 6 is satisfied.

Objective 7 states that the spacecraft software shall accept data for transmission from a buffer that is easily accessible to a user. This refers to the communication between nanoMCS and the PC. Downloaded logs from the spacecraft showed correct timestamps and off-nadir angle during the capture. This demonstrates that both scheduling an upload and pulling downloaded data through the nanoMCS are available to the user in a straightforward manner. Therefore, we can conclude that this objective is satisfied.

Objective 8 states that HYPSON-1 shall avoid imaging during complete cloud cover, excessive white caps, and the turbulent atmosphere. One of the main issues with mission planning was cloud coverage, as suspected clear weather would suddenly change after the capture mission was scheduled. This would result in a cloudy image and therefore be almost unusable for analysis. The satellite does not have unlimited storage space, so it is necessary to download and delete the data as soon as possible after capture. Unusable captures would, therefore, take time and storage space, which should have been used in an area with less cloud coverage. As there are currently no detection algorithms for these scenarios, Objective 8 was not satisfied.

Objectives 9 and 10 are requirements concerning downlink size and duration over NTNU through the S-band. They state that the L1A data products shall be downlinked in less than 24 hrs, with no more than 2200 frames and file size less than 420 *MB*. L1A data is reconstructed, raw instrument data [53] downlinked directly from the satellite. The downlink speed depends on the file size and the satellite's elevation. The elevation varies between about 4° and 90° throughout the day, where the signal duration and strength are increased when the satellite is closer to zenith. The metazip folder file size was 792 *kB* and was relatively small because it only contained telemetry and logs. In comparison, the compressed cube file had a file size of 66,5 *MB*, thus, it is the downlink we will focus



---

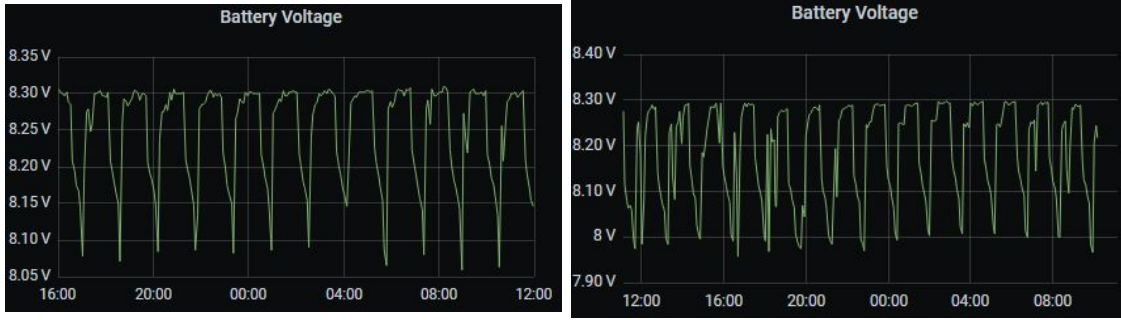
on. The compressed cube took 11 minutes to downlink during AOS, equal to 3 hours, 4 minutes, and 17 seconds since the capture end. Considering that the image was taken during a downlink pass, we had to wait for another AOS before it started downlinking again. This is calculated as the time it takes HYPSON-1 to orbit the Earth (90 minutes) minus the duration of AOS (10 minutes on average). Thus, one could argue that the downlink duration since the capture end was closer to 1 hour, 44 minutes, and 17 seconds. Also, the "timestamps\_services" log file from the metazip states that we had 955 frames during the capture. These findings suggest that both Objectives 9 and 10 are satisfied with a substantial margin.

Objective 11 states that housekeeping telemetry data shall be downloaded at least once per day. This telemetry is used to monitor the functioning and health of HYPSON-1. Such telemetry is downloaded for every pass and can be observed on Grafana as the satellite enters Loss Of Signal (LOS). We can check for any reboots in the instruments and the battery voltage there. This ensures that the operators have essential information about the satellite's health. We can therefore conclude that Objective 11 is satisfied.

Objective 12 requires that the target area size is less than  $100 \times 100 \text{ km}^2$ , that the location is in specific places such as Mid-Norway fjords and coast, and that the imaging period is between 06:00 AM and 13:00 PM Local Time in the spring and summer season. Georeferencing suffered from improper time synchronization, thus, we were not able to acquire an accurate target area size. The first part of the requirement is therefore not satisfied. Furthermore, we know that the capture were over Frohavet, which is in Mid-Norway. The local capture time of the center point was 12:24:21.5 UTC+2, thus, the last two requirements are satisfied. However, it should be stated that HYPSON-1 also images targets at later hours during the day as long as enough sunlight strikes the area.

Objective 13 states that the satellite should be operational for at least five years with weekly mission updates. First, there have been weekly mission updates on HYPSON-1 since February. Second, we have to check the battery voltage to determine if the satellite's health is in good enough condition to be operational for five years. We stated in chapter 4.1.6 that if the voltage dropped below 7 V, then the battery would be at a critical level, while everything above 7.6 V was considered operational. Below 7.6 V would require the battery to charge up more before one could operate on the satellite. The battery voltage from the 17th of May can be inspected in Grafana by looking at the battery voltage in Figure 27. The battery voltage from about the 17th of February and the 6th of July are included below in Figure 54 to compare any voltage drop in the first six months since launch. The minimum battery voltage was about 8.05 V in February, 7.95 V in May, and 7.98 V in July. The maximum voltage was about 8.30 V throughout the months, which means that the battery charged almost to max each pass. This indicates that the voltage fluctuates at a healthy level, that the battery charges correctly, and that the weekly missions do not wear out the battery. Therefore, by looking solely at the EPS battery, we predict that HYPSON-1 will be operational more than five years with weekly mission updates. Objective 13 is so far satisfied.

Objective 24 regarding georeferencing has been stated above to be inaccurate due to improper time synchronization during capture. The HYPSON team is working on solving this issue and will hopefully be ready shortly. Thus, the objective is currently not satisfied.



(a) Battery voltage on the 16th to 17th of February. (b) Battery voltage on the 5th to 6th of July.

**Figure 54:** HYPPO-1 EPS battery voltage from Grafana.

## 6.2 Calibration and conversion

### 6.2.1 Calibration

The spectral calibration experiment conducted in chapter 2.5.4 was not an ideal experimental setup compared to using a more expensive Lambertian surface. However, for demonstration purposes, one could argue that it was sufficient. It explains the methods used to do spectral calibration, which then was applied to the Frohavet capture. Radiometric calibration was also applied to the data, converting the pixel count in digital numbers captured by the HSI sensor to the ToA radiance. The left image in Figure 35 shows the RGB composite of Frohavet before calibration, whereas Figure 38 shows after. A difference between these images is the saturation, as land and ocean look clearer after calibration. However, the snow is oversaturated, exposing lines in the image. These lines are due to more incident photons being captured along the slit width of the sensor. When further applying classification algorithms and PCA, such lines could dominate the spectral values, causing them to be the main focus in the clusters and principal components. Furthermore, even after applying a mask on the oversaturated snow, these lines would persist in the ocean, although harder to spot in the RGB composite.

Figure 48 shows the spectrum of an ocean pixel from Frohavet before and after calibration with the mentioned methods. The first and last spectral pixels in the uncalibrated data were given by the center part of the sensor. These were equal to the spectral pixel numbers 428 and 1508 with a *bin factor* of 9, which resulted in 120 spectral pixels. This was the same amount as the number of HSI bands. As a result of binning the values, the intensity was divided by the binning factor to get the average for each bin.

The first four bands, 388.04, 391.59, 395.13, and 398.67 *nm*, had zero radiance values as the sensor is designed to acquire radiance values in the spectral range 400-800 *nm*. These were therefore excluded from the resulting graphs.

The above result demonstrated three things. First, the spectral pixels were successfully calibrated to match the required spectral range. Second, the radiance values showed spectral signatures such as the absorption line for oxygen  $O_2$  at 760 *nm*, supporting the applicability of these calibration methods. The third was the need for a calibration method to remove spectral lines in the images. Because of a lack of atmospheric correction and Smile and Keystone correction at the time, precise radiance values could not be obtained. Although, it could still indicate whether or not the radiance to reflection conversion was successful.

---

## 6.2.2 Requirements of calibration

Objective 14 requires HYPSON-1 to use standard radiometric and spectral calibration methods. Our findings indicate that the calibrated values were correct, thus satisfying the objective.

## 6.2.3 Radiance to reflectance conversion

We ensured a close to nadir capture with a max elevation of  $89.211^\circ$ , as precise radiance values could not be obtained through calibration. Thus, limiting the amount of atmosphere as a lower angle would result in a greater distance between the HSI and the target. Nevertheless, with an altitude of about  $500\text{ km}$ , there was still a significant amount of atmosphere between the objects. Although, we could still get an indication of whether or not the radiance to reflectance conversion was successful.

The solar spectral irradiance  $E_0$  for each hyperspectral band was not available at the time of writing this thesis. Neither were the solar zenith angle  $\theta$  for each pixel. Thus, we had to make two assumptions. First, we could acquire the solar spectral irradiance from a satellite with a similar orbit and spatial resolution as HYPSON-1. Second, we had to acquire the solar zenith angle for the target center at the time of capture and use that angle for the rest of the pixels. The NASA-PACE satellite would suffice for the solar spectral irradiance. The NASA-PACE has a similar orbit to HYPSON-1, but with an altitude of  $676.6\text{ km}$ , whereas HYPSON-1 has an altitude of  $525\text{ km}$ . Thus, the amount of solar irradiance is higher than expected as the satellite is closer to the Sun. However, as the distance from the Earth to the Sun is  $149\,600\,000\text{ km}$ , one could argue that this error is insignificant. Also, the spatial resolution had a difference of  $1\text{ mm}$  between the satellites, meaning we had to conduct an interpolation of the irradiance values. As this was a linear interpolation, minor errors in irradiance could occur.

For ideal measurements, the solar zenith angle should be obtained for each captured pixel. As this was not possible at this time due to limitations in HYPSON, we focused on the center pixel instead. This center pixel had the wrong coordinates, as stated above, however, since it is close to the actual one, we determined that it was sufficient to use it as a reference for the solar zenith angle.

The solar zenith angle of the logged coordinates at their respective time of capture could indicate the error we gain, by using the center pixel. Capture start and end had a solar zenith angle of  $47.2653^\circ$  and  $47.0294^\circ$ . This results in an error of  $0.2359^\circ$  from start to stop.

## 6.2.4 Requirements of radiance to reflection conversion

This requirement was custom made for this thesis as conversion to reflectance is essential for proper analysis, and was not found in the "HYPSON-1 requirements" sheet. The first process of converting digital values to radiance was a success as described above, however, conversion to reflectance has its limitations.

We acknowledge that there are numerous errors during this conversion. The solar spectral irradiance was taken from another sensor with a different spatial resolution and altitude. The solar zenith angle was obtained for the center pixel instead of for each one, and the radiance values lack both atmospheric and Smile and Keystone correction. However, only

---

the magnitude is the main difference from actual reflectance values, as the results should show familiar spectral traits. Thus, we can get an indication of whether the conversion worked or not. Figure 52b shows the spectral signatures in reflectance for each cluster after classification. The values are in percentages, and the spectral signatures are almost identical with the radiance values, with spectral traits such as the  $O_2$  absorption line. Also, the magnitude of the values represent percentages, with 15 % reflectance as the highest point. This supports the idea that with correct variables from HYPSON-1, we could get the actual reflectance with this conversion. Objective 23 is, however, not satisfied.

## 6.3 Analysis

### 6.3.1 Unsupervised classification

The results from the unsupervised classification of the Frohavet scene with 10 and 8 clusters as output are depicted in Figures 49a and 49b. This analysis indicates that using the k-means classification results in an image divided into clusters. The cluster with the highest frequency was the ocean, while snow and clouds were divided into several clusters. We mainly wanted to focus the analysis on the ocean, so we decided to mask the rest. Also, there is little variance in the two clustered images, except more focus on cirrus clouds when there are 10 clusters. With this information, we chose to analyze with 8 clusters further, as the cirrus clouds would be masked out either way.

We chose to be strict with what spectral values we wanted to analyze, such that there were minimal amounts of cirrus clouds, islands, and shores. This is due to such objects interfering with the ocean's spectral values in classification and PCA. We carefully analyzed each of the pins in Figure 40 to not choose a wavelength that could indicate algae concentration. Therefore, band 76, representing wavelength 651  $nm$ , was chosen to distinguish the ocean from the other objects. This wavelength was outside the two absorption peaks for chlorophyll, as depicted in Figure 8. The resulting classified image in Figure 51a shows 8 clusters, where cluster 8 can be determined as shores by looking at Figure 52a. This is reasonable as we only used one wavelength to mask the whole area, thus, expecting some interference by other objects than ocean. The rest of the pixels show the colors of the ocean.

Unfortunately, the lines that were not removed in calibration appears in almost all the clusters. This is a source of error for unsupervised classification as the algorithm focuses on both camera artifacts and the ocean spectra. This could result in invalid cluster representation, as can be seen for cluster 5. This cluster represents one of the ocean colors as well as vertical lines on the left hand side of the image. Therefore, we can not be certain that the reflection of these clusters give valid information about the ocean colors.

To remove potential stray light and other spectral artifacts, we subtracted the mean ocean reflectance spectra from each cluster spectra, resulting in Figure 52c. One could argue that cluster 7 classify shallow water, as its reflectance is much higher than the others after about 720  $nm$ , similar to cluster 8, while the rest are deep ocean water. No reflectance peaks in the wavelengths 465 or 665  $nm$  indicate either meager amounts of chlorophyll-a or none. However, even though we did not detect any algae with k-means, the experiment's results found clear support for the usage of unsupervised classification for clustering the ocean's spectral signatures.

---

### 6.3.2 PCA

The first PCA was done on the whole Frohavet scene, exposing the layers of snow, land, clouds, and ocean. This PCA was conducted as a test to see how well it performed on differentiating objects, which it did. However, the ocean colors were not highlighted as they were shadowed by larger spectral radiance values from the other objects. Thus, we created an ROI over the ocean, which was rerun through the PCA. Then we composed the RGB images with the first three components, as they were the eigenvectors containing the most information.

The results demonstrated two things. First, Figure 50b depicts the resulting ocean colors. These colors highlight water close to shores and clouds, as well as the deep ocean. Second, camera artifacts such as vertical lines were even more apparent than with classification. These artifacts were much less visible when we did not apply the mask, as the spectral radiance of other objects was more distinctive. The applicability of PCA on the ocean without atmospheric correction, Smile and Keystone correction, and removal of the camera artifacts leads to a noisy image. Therefore, we cannot confidently say how well the ocean colors, such as chlorophyll-a, are represented. However, the PCA might have helped reduce the size of the data.

The 120 bands from the HSI resulted in a large time complexity when analyzing due to the high amount of data. The PCA reduces the number of bands needed to extract information about the captured data. SNAP sorted the PCA components by their eigenvalues in descending order. This resulted in components 1 to 3 having the highest correlation, storing the most information. To check whether or not these components could be used to represent the real data, we ran them through the unsupervised classification and analyzed the results. Figure 51b depicts the resulting image, while Figure 51d shows the frequency of each cluster. By comparing the classification with and without PCA, we could see that the classified images were similar to a high degree. The frequency of the clusters was almost the same, differentiating between  $\pm 1.5\%$ . Thus, there was little to no variation in running k-means on our data with and without PCA. The advantage of running PCA first was that the k-means computation time was reduced from 61 seconds to 6 seconds, as we were reducing input bands from 120 to 3.

We can conclude that reducing the dimension of our data from reduces the computation time of our classification algorithm to about one-tenth of the original computation time. PCA drastically reduces the amount of data while still containing the same information, thus, proving to be a useful tool for hyperspectral data analysis.

### 6.3.3 Requirements of analysis

Objective 15 states that the 3D image reconstruction of the HSI frames shall have at least 5 *nm* spectral resolution in the 400-800 *nm* spectral range. The spectral resolution of the HSI is 3.54 *nm* in the specified spectral range, thus, the requirement is satisfied. We can also conclude that objective 16 is satisfied as we have 120 spectral bands in the VIS-NIR range.

Objective 17 states that the downlinked L1A data should contain detectable optical signatures such as chlorophyll-a that can be processed on the ground. The term L1A is described above in the discussion about Objectives 9 and 10. Both classification and PCA displays the ocean colors. However, the distinctive spectral signatures that are highlighted

---

in both analysis methods are heavily influenced by camera artifacts and atmosphere. To determine whether this requirement is fulfilled, we have to apply atmospheric correction, Smile and Keystone correction, and removal of camera artifacts. A suggestion for how the latter can be conducted will be introduced in section "Further work." Nevertheless, objective 17 can not be concluded as satisfied at this time.

Objective 18 states that operational data shall be useful for decision-making and in-situ validation with autonomous agents. It is also challenging to determine whether or not this requirement is satisfied, as decision-making and in-situ validation focus on optical signatures. As long as uncalibrated noise is in the data, such usage is not available. Thus, it remains unclear if this requirement is satisfied.

The first part of Objective 19 requires HYPSON-1 to acquire hyperspectral images over target areas with the highest probability of detection off the coast of Norway. The second part requires off-nadir pointing capability. Frohavet lies by the coast in Mid-Norway and is one of the target areas in Norway with the most anticipation when it comes to detecting algae. This is supported by the fact that robotic agents from NTNU's Mission Control Center, ASV, AUV, and UAV, are already deployed in Frohavet for in-situ measurements [1]. The acquired image had a max elevation of  $89.252^\circ$  which is close to nadir pointing. However, we could have chosen another pass, which would have had a lower elevation. This would result in more atmosphere and be therefore not desirable. Thus, we can conclude that Objective 19 is satisfied.

Objective 20 states HYPSON shall provide and support ocean color mapping through a Hyperspectral Imager (HSI) payload, autonomously processed data, and on-demand autonomous communications in a concert of robotic agents at the Norwegian coast. We did have ocean color mapping through an HSI payload, but only parts of the data was autonomously processed. We still require radiometric and spectral calibration, as well as the mentioned atmospheric and Smile and Keystone corrections, to be automatic and ready for end-users. Thus, Objective 20 is not satisfied.

Objective 21 has several requirements for HYPSON-1, such as enabling atmospheric correction, dimensionality reduction, spectral compression, classification, and target detection. We have confirmed that dimensionality reduction with PCA and classification with the k-means algorithm was successful. Atmospheric correction was not applied as this calibration method was not available from the HYPSON team, while target detection was not a focus during this thesis. Thus, we can so far conclude that HYPSON-1 enables dimensionality reduction and classification, while the rest needs further research.

Objective 22 simply ensures that the target's solar zenith angle shall be less than 75 degrees. The Frohavet capture used in this thesis had a solar zenith angle of  $45.4^\circ$ , thus confirming that this objective is satisfied.

## **6.4 Software used - STK, SNAP, and Excel**

### **6.4.1 Mission planning with STK**

STK worked great for target capture planning. The software visualizes HYPSON-1's orbit and the target location, and calculates the time of max elevation and velocity and position vectors. However, STK was somewhat time-consuming when planning a mission for several days. The software did not calculate quaternions, so we had to extract all values into the quaternion Matlab script. Then we manually typed the quaternions into the terminal to

---

generate the FC and PC scripts. This took too much time and made room for manual errors. Therefore, it is necessary to produce a more automated process to reduce the amount of manual labor.

Furthermore, this automation should include updating the quaternions and the Unix timestamps regularly for upcoming captures, as it has been shown that STK produces errors if the planned capture is several days in advance. Master students at NTNU created the first process for this. They have worked on "Satellite Operations User Interface Enhancement Suite" (SOUIES), where quaternions and PC/FC scripts can be made directly in the software, thus, replacing STK completely.

#### 6.4.2 SNAP

The decompressed ".bip" file with its respected ".hdr" file was imported to Sentinel Application Platform (SNAP), a software program ideal for Earth Observation processing and analysis [54]. The RGB composite of the hyperspectral pushbroom image was created by combining the bands 70 (Red), 47 (Green), and 27 (Blue), corresponding to the wavelengths 630 nm, 550 nm and 480 nm, respectively.

The spectrum view and pin placement tools let us acquire and visualize the pixel spectral radiance of each band. By choosing objects such as snow, land, clouds, and the ocean, we could determine what wavelengths differentiated our object of interest from the rest. SNAP's masking tool was then used to mask this ROI. We had now reduced the area that would be analyzed further, which is essential when working with hyperspectral data processing.

Unsupervised classification with the k-means algorithm and PCA were two tools applied to the data. We determined the number of output clusters/components, what bands to use as input, and the region of interest. The output images show the ocean colors represented by their specific spectral radiance values.

As for PCA, it was only possible to extract the eigenvectors and not the eigenvalues. The eigenvalues would have shown us the amount of information each principal component contained, which would result in more accurate results. Neither was it possible to edit the pixel spectral radiance values practically, as we wanted to average the values over each column of pixels to remove camera artifacts.

SNAP was an excellent software for analyzing and processing hyperspectral data. Applying data processing techniques efficiently and practically is crucial when working with extensive data. SNAP is a free-to-use software that saves its end-user both time and resources.

#### 6.4.3 Excel

We exported the values for wavelength, radiance, and principal components from SNAP into Excel as Comma-separated values files (CSV). Excel is also an efficient way of processing and visualizing large amounts of data. The "line charts" that were created represented the diversity between the values transparently, which was easy for the end-user to analyze. To get the correct solar irradiance values, interpolating the NASA-PACE and HSI wavelengths was done with *FORECAST.LINEAR*. The linear interpolation function predicted a value based on existing values along a linear trend[50], which was a valid method for this task. Excel was also used for basic mathematical operations to convert radiance to reflectance.

---

## 7 Conclusion

The months after HYPPO-1 was launched into orbit were spent on satellite operations to observe housekeeping telemetry, and acquire images over areas of interest. The Frohavet capture analyzed in this thesis was one of many captures acquired during operations. However, it was chosen due to low cloud coverage and close to nadir pointing. As the first person in HYPPO to go through the whole process of planning, acquiring, and analyzing a capture, made it possible to choose the best possible capture scenario based on the area's weather and satellite's pointing. It was a valuable experience for both the HYPPO team and as a student.

### 7.1 Findings

Mission planning with STK and Matlab met the operation needs for obtaining correct satellite pointing and capture timestamps. However, the satellite TLEs were not updated when planning for several days in advance. Thus, regular mission planning was necessary, which was time-consuming. Monitoring the HYPPO-1 systems through nanoMCS and hypso-cli made it accessible to operate on the satellite's subsystems and communicate with the OPU. Also, with high bit rate down-linking of housekeeping telemetry and logs, the operators could regularly observe the satellite's health and troubleshoot any problems. The captured area corresponded to the mission planning according to the logged timestamps and off-nadir angle. However, correct georeferencing must be in order to determine the camera's exact precision. The captured hyperspectral data were successfully calibrated with both spectral and radiometric calibration to get the correct spectral range and radiance values. The radiance to reflectance conversion suffered from limitations, as measurements were gathered from different sources than HYPPO-1. Nevertheless, the reflection values had correct magnitude and showed well-known spectral signatures, supporting the idea that correct measurements will get accurate results with this method. Neither k-means nor PCA detected any chlorophyll-a in the spectra, however, we predict that this is due to camera artifacts that became more apparent after creating a region of interest over the ocean. These vertical lines might have overshadowed any potential algae concentration, resulting in a less accurate analysis. However, PCA was successfully applied for dimensionality reduction, while classification successfully clustered the data based on the spectral values. This proves the two methods' applicability to large quantities of hyperspectral data.

### 7.2 Future work

HYPPO needs to put resources into transitioning from STK to the more automated mission planning with SOUIES. This will reduce manual labor and errors and provide the most updated TLEs for upcoming captures. It is crucial for the operators that time synchronization and georeferencing are correct, such that the accuracy of the captures can be determined. For HYPPO-1 data to be available for end-users and satisfy requirements, HYPPO needs to put resources into two things. First, correct atmospheric and Smile and Keystone corrections, and conversion of radiance to reflectance. The latter is dependent on correct radiance values, solar zenith angle  $\theta$  per captured pixel, and solar spectral irradiance  $E_0$  per spectral band. Accurate reflectance measures are essential prerequisites for any analysis methods, and should be updated more specifically as an objective for HYPPO. Second, camera artifacts has to be removed by e.g. removing the average spectra of each column of data. This could reduce the noise and ensure more accurate PCA and



---

classification results.

---

## Bibliography

- [1] Grotte, Mariusz E. and Birkeland, Roger and Honore-Livermore, Evelyn and Bakken, Sivert and Garrett, Joseph L. and Prentice, Elizabeth F. and Sigernes, Fred and Orlandic, Milica and Gravdahl, J. Tommy and Johansen, Tor A. *Ocean Color Hyperspectral Remote Sensing With High Resolution and Low Latency—The HYPSON-1 CubeSat Mission*. 2022.
- [2] HYPSON team. *Files from NanoAvionics visit*. en.
- [3] Jose M. Bioucas-Dias et al. *Hyperspectral Remote Sensing Data Analysis and Future Challenges*. en. 2013.
- [4] Fredrik Gran-Jansen. *Hyperspectral data analysis for chlorophyll estimation*. en. 2021.
- [5] HYPSON team. *HYPSON-1 Requirements*. en.
- [6] *What is remote sensing and what is it used for?* Accessed: 15.11.2021. URL: [https://www.usgs.gov/faqs/what-remote-sensing-and-what-it-used?qt-news\\_science\\_products=0qt-news\\_science\\_products](https://www.usgs.gov/faqs/what-remote-sensing-and-what-it-used?qt-news_science_products=0qt-news_science_products).
- [7] Elizabeth Prentice. *Hyperspectral Lab, TTK4265 Optical Remote Sensing*. Oct. 2021.
- [8] Bruce Hapke. *Reflectance Spectroscopy - an overview*. URL: <https://www.sciencedirect.com/topics/agricultural-and-biological-sciences/reflectance-spectroscopy>.
- [9] F.Vasefi. *Hyperspectral Imaging - an overview*. URL: <https://www.sciencedirect.com/topics/medicine-and-dentistry/hyperspectral-imaging>.
- [10] *What is hyperspectral imaging?* <https://www.specim.fi/library/what-is-hyperspectral-imaging/>. Accessed: 15.11.2021.
- [11] Fred Sigernes. *Basic Hyper Spectral Imaging*. Lecture notes used in the course TTK4265: Optical Remote Sensing.
- [12] Prentice, Elizabeth Frances and Grøtte, Mariusz Eivind and Sigernes, Fred and Johansen, Tor Arne. “Design of a hyperspectral imager using COTS optics for small satellite applications”. In: *International Conference on Space Optics — ICSSO 2020*. Vol. 11852. SPIE, June 2021, pp. 2154–2171. URL: <https://www.spiedigitallibrary.org/conference-proceedings-of-spie/11852/1185258/Design-of-a-hyperspectral-imager-using-COTS-optics-for-small/10.1117/12.2599937.full>.
- [13] Fred Sigernes et al. “Do it yourself hyperspectral imager for handheld to airborne operations”. In: *6021-6035* (2018). ISSN: 1094-4087. URL: <https://ntnuopen.ntnu.no/ntnu-xmlui/handle/11250/2579680>.
- [14] Michael T. Eismann. *Hyperspectral Remote Sensing*.
- [15] Omkar S N, Meghana Sudhindra, and ashokavanjare. *Hyperspectral Signal Processing to Identify Land Cover Pattern*. July 2014.
- [16] Emmanuel Christophe and P. Duhamel. “Hyperspectral image compression: Adapting SPIHT and EZW to anisotropic 3-D wavelet coding”. In: *IEEE transactions on image processing : a publication of the IEEE Signal Processing Society* 17 (Jan. 2009), p. 2334. DOI: 10.1109/TIP.2008.2005824.
- [17] Platt, T., Hoepffner, N., Stuart, V. and Brown, C. (eds.) *Why Ocean Colour? The Societal Benefits of Ocean-Colour Technology*. Reports of the International Ocean-Colour Coordinating Group, No. 7, IOCCG, Dartmouth, Canada. IOCCG (2008).
- [18] Nasa Science. *Ocean Color*. en. URL: <https://science.nasa.gov/earth-science/oceanography/living-ocean/ocean-color>.

- 
- [19] US Department of Commerce, National Oceanic and Atmospheric Administration. *Can we clean up, stop, or end harmful algal blooms?* URL: <https://oceanservice.noaa.gov/facts/hab-solutions.html>.
- [20] Wikipedia contributors. *Chlorophyll*. Online; accessed 16-December-2021. 2021. URL: <https://en.wikipedia.org/w/index.php?title=Chlorophyll&oldid=1059613242>.
- [21] Oyama, Yoichi and Matsushita, Bunkei and Fukushima, Takehiko and Nagai, T. and Imai, Akio. *A new algorithm for estimating chlorophyll-a concentration from multi-spectral satellite data in case II waters: A simulation based on a controlled laboratory experiment*. Apr. 2007. DOI: 10.1080/01431160600975295.
- [22] Synopsys. *Stray Light*. URL: <https://www.synopsys.com/glossary/what-is-stray-light.html>.
- [23] Naoto Yokoya, Norihide Miyamurab, Akira Iwasaki. *Preprocessing of hyperspectral imagery with consideration of smile and keystone properties*. URL: [https://www.researchgate.net/figure/Smile-and-keystone-properties\\_fig2\\_253205974](https://www.researchgate.net/figure/Smile-and-keystone-properties_fig2_253205974).
- [24] GISGeography. *What is Atmospheric Correction in Remote Sensing?* Nov. 2015. URL: <https://gisgeography.com/atmospheric-correction/>.
- [25] Xiujuan Yu et al. *Laboratory spectral calibration and radiometric calibration of hyper-spectral imaging spectrometer*. en. 2014.
- [26] *Fluorescent lighting spectrum peaks labeled with coloured peaks added*. [https://commons.wikimedia.org/wiki/File:Fluorescent\\_lighting\\_spectrum\\_peaks\\_labeled\\_with\\_colored\\_peaks\\_added.png](https://commons.wikimedia.org/wiki/File:Fluorescent_lighting_spectrum_peaks_labeled_with_colored_peaks_added.png). Accessed: 12.11.2021.
- [27] Rodarmel, Craig and Shan, Jie. *Principal Component Analysis for Hyperspectral Image Classification*. en. Jan. 2002.
- [28] *Radiance*. <https://en.wikipedia.org/w/index.php?title=Radiance&oldid=1050148471>. Page Version ID: 1050148471. Oct. 2021.
- [29] *Steradian*. Page Version ID: 1042816326. Sept. 2021. URL: <https://en.wikipedia.org/w/index.php?title=Steradian&oldid=1042816326>.
- [30] ESA. *SNAP Data Processors - Radiance-To-Reflectance Conversion Algorithm Specification*. URL: [seadas.gsfc.nasa.gov/help-8.2.0/rad2refl/Rad2ReflAlgorithmSpecification.html](https://seadas.gsfc.nasa.gov/help-8.2.0/rad2refl/Rad2ReflAlgorithmSpecification.html).
- [31] *Solar zenith angle*. en. 2021. URL: [https://en.wikipedia.org/wiki/Solar\\_zenith\\_angle](https://en.wikipedia.org/wiki/Solar_zenith_angle).
- [32] *Solar Zenith Angle*. en. Mar. 2011. URL: <https://sacs.aeronomie.be/info/sza.php>.
- [33] Sivert Bakken. *Development of a Small Satellite with a Hyperspectral Imaging Payload and Onboard Processing for Ocean Color*. en. Mar. 2022.
- [34] HYPSON team. *HYPSON-1 Bus*. en.
- [35] Wikipedia contributors. *Magnetorquer* — *Wikipedia, The Free Encyclopedia*. [Online; accessed 4-July-2022]. 2022. URL: <https://en.wikipedia.org/w/index.php?title=Magnetorquer&oldid=1070942783>.
- [36] NanoAvionics. *NanoAvionics Star TrackerST-1*.
- [37] *Reaction wheel*. en. May 2022. URL: [https://en.wikipedia.org/w/index.php?title=Reaction\\_wheel&oldid=1090153495](https://en.wikipedia.org/w/index.php?title=Reaction_wheel&oldid=1090153495).
- [38] Yong Bai, Qiang Bai. *Subsea Engineering Handbook (Second Edition)*. 2019. URL: <https://www.sciencedirect.com/topics/engineering/magnetometer>.
- [39] Santamaría, Germán. *How sun sensors work*. en-US. Sept. 2021. URL: <https://www.solar-mems.com/how-sun-sensors-work/>.
-

- 
- [40] Hywel Curtis. *An overview of satellite Electrical Power Systems (EPS) on the global marketplace for space*. en. Mar. 2022. URL: <https://blog.satsearch.co/2020-06-10-satellite-electrical-power-systems-eps-on-the-global-marketplace-for-space>.
- [41] HYPPO team. *PC/FC scripting for HYPPO-1*. en.
- [42] HYPPO team. *Manual for HYPPO-1*. en.
- [43] Satlab. *Full-duplex High-Speed S-band Transceiver*. URL: <https://www.satlab.com/products/srs-4/>.
- [44] *Horizontal coordinate system*. en. Mar. 2022. URL: [https://en.wikipedia.org/w/index.php?title=Horizontal\\_coordinate\\_system&oldid=1079858012](https://en.wikipedia.org/w/index.php?title=Horizontal_coordinate_system&oldid=1079858012).
- [45] Ansys Government Initiatives (AGI). *Systems Tool Kit (STK)*. en. URL: <https://www.agi.com/products/stk>.
- [46] Zizung Yoon, Karsten Grojckatthöfer. *Introduction into quaternions for spacecraft attitude representation*. en. May 2021. URL: <http://www.tu-berlin.de/fileadmin/fg169/miscellaneous/Quaternions.pdf>.
- [47] Mariusz Eivind Grøtte et al. “Spacecraft Attitude and Angular Rate Tracking using Reaction Wheels and Magnetorquers”. In: *IFAC-PapersOnLine* (2020).
- [48] Wikipedia contributors. *Plankton, Aerosol, Cloud, ocean Ecosystem*. en. 2022. URL: [https://en.wikipedia.org/wiki/Plankton,\\_Aerosol,\\_Cloud,\\_ocean\\_Ecosystem](https://en.wikipedia.org/wiki/Plankton,_Aerosol,_Cloud,_ocean_Ecosystem).
- [49] Ocean Color Web. *Spectral Characterization Data by Sensor*. en. URL: [https://oceancolor.gsfc.nasa.gov/docs/rsr/rsr\\_tables/](https://oceancolor.gsfc.nasa.gov/docs/rsr/rsr_tables/).
- [50] Dave Bruns. *How to use the Excel FORECAST function*. Online; accessed 17-December-2021. URL: <https://exceljet.net/excel-functions/excel-forecast-function>.
- [51] University of Oregon Solar Radiation Monitoring Laboratory. *Solar position calculator*. en. Mar. 2022. URL: <http://solardat.uoregon.edu/SolarPositionCalculator.html>.
- [52] Wikipedia contributors. *Two-line element set — Wikipedia, The Free Encyclopedia*. en. 2022. URL: [https://en.wikipedia.org/w/index.php?title=Two-line\\_element\\_set&oldid=1091170389](https://en.wikipedia.org/w/index.php?title=Two-line_element_set&oldid=1091170389).
- [53] Earth Data. *Data Processing Levels*. en. July 2021. URL: <https://www.earthdata.nasa.gov/engage/open-data-services-and-software/data-information-policy/data-levels>.
- [54] *Scientific Image Processing Toolbox*. Accessed: 15.11.2021. URL: <https://www.brockmann-consult.de/portfolio/earth-scientific-image-processing/>.

